Projection-specific integration of convergent thalamic and retrosplenial signals in the presubicular head direction cortex

Authors

Louis Richevaux[1]*, Dongkyun Lim[1], Mérie Nassar[1], Léa Dias Rodrigues[1], Constanze Mauthe[1], Ivan Cohen[3], Nathalie Sol-Foulon[2], Desdemona Fricker[1,4]*

[1]Université Paris Cité, CNRS, Integrative Neuroscience and Cognition Center, F-75006 Paris, France, [2]Sorbonne Université, INSERM, CNRS, Paris Brain Institute, ICM, Pitié-Salpêtrière Hospital, F-75013 Paris, France, [3]Sorbonne Université, INSERM, CNRS, Neuroscience Paris Seine, Institut de Biologie Paris Seine, F-75005 Paris, France, [4]Lead contact.

Correspondence: desdemona.fricker@parisdescartes.fr, louis.richevaux@parisdescartes.fr

Summary

Head-direction (HD) signals function as the brain's internal compass. They are organized as an attractor, and anchor to the environment via visual landmarks. Here we examine how thalamic HD signals and visual information from the retrosplenial cortex combine in the presubiculum. We find that monosynaptic excitatory connections from anterior thalamic nucleus and from retrosplenial cortex converge on single layer 3 pyramidal neurons in the dorsal portion of mouse presubiculum. Independent dual wavelength photostimulation of these inputs in slices leads to action potential generation preferentially for near-coincident inputs, indicating that layer 3 neurons can transmit a visually matched HD signal to medial entorhinal cortex. Layer 4 neurons, which innervate the lateral mammillary nucleus, form a second step in the association of HD and landmark signals. They receive little direct input from thalamic and retrosplenial axons. We show that layer 4 cells are excited di-synaptically, transforming regular spiking activity into bursts of action potentials, and that their firing is enhanced by cholinergic agonists. Thus, a coherent sense of orientation involves projection specific translaminar processing in the presubiculum, where neuromodulation facilitates landmark updating of HD signals in the lateral mammillary nucleus.

Keywords

Keywords: postsubiculum, presubiculum, head direction, multisensory, dendritic integration, circuit mechanism, patch clamp, brain slices, layer specific, projection specific

Introduction

The head direction (HD) system functions as the brain's compass system. It is distributed across several interconnected brain structures, and hierarchically organized from the brainstem to the lateral mammillary nucleus (LMN; Stackman and Taube, 1998), the anterior thalamic nuclei (ATN; Taube, 1995), and the dorsal Presubiculum (PrS; Ranck, 1984; Taube et al., 1990a). Modeling work suggests the HD system functions as a ring attractor, where the population of HD neurons is arranged in a one dimensional manifold (Blair and Sharp, 1995; McNaughton et al., 2006; Skaggs et al., 1995). The activity of thalamic and PrS HD neurons is correlated across different brain states, even during sleep, independently of sensory cues (Peyrache et al., 2015). The bump-like activity dynamics of an attractor network can maintain HD signals based on excitatory-excitatory or excitatory-inhibitory interactions (Knierim and Zhang, 2012; Simonnet et al., 2017). However, HD signals may drift in the dark (Taube et al., 1990b; Zugaro et al., 2003). For precise navigation, internally generated information on head direction must be combined with awareness of location in an environment. Mechanisms underlying the combination of egocentric head direction signals with anchoring to allocentric landmarks remain to be clarified.

Head direction and visual landmark signals may be integrated in the presubiculum (Jeffery et al., 2016; Yoder et al., 2019). Head direction cells are found in the superficial and deep layers of dorsal presubiculum, also termed postsubiculum (Boccara et al., 2010), and most layer 3 neurons in the dorsal presubiculum are head direction cells (Tukker et al., 2015; Preston-Ferrer et al., 2016). These cells receive monosynaptic head direction inputs from the anterior thalamus (Nassar et al., 2018; Peyrache et al., 2015; Balsamo et al., 2022). Lesions of the PrS impair the visual landmark control of a cell's preferred direction in ATN and in LMN (Goodridge and Taube, 1997; Yoder et al., 2015). Presubicular lesions also induce place field instability in the hippocampus (Calton et al., 2003), suggesting this region may be crucial to the anchoring of directionally modulated neurons to environmental landmarks.

Landmark based navigation depends on reliable visual cues. The PrS appears to receive direct projections from the primary visual cortex and indirect visual input via the retrosplenial cortex (Van Groen & Wyss 2003; Vogt & Miller 1983). The retrosplenial cortex encodes angular head velocity (Alexander & Nitz 2015; Keshavarzi et al. 2022) and visual landmark information (Auger et al., 2012; Clark et al., 2010; Sit and Goard, 2023), and supports an array of cognitive functions including memory, spatial and non-spatial context and navigation (Vann et al., 2009; Vedder et al., 2017). In particular, some neurons in the dysgranular retrosplenial cortex encode landmark-dominated head-direction signals (Jacob et al., 2017). Presubicular layer 3 cells receiving projections from both the anterior thalamus and the retrosplenial cortex (Kononenko and Witter 2012) could update the compass and bind landmarks to head direction signals. Presubicular neurons could then broadcast integrated HD-landmark signals directly to the MEC, via deep layers to the ADN and via layer 4 neurons to the LMN (Huang et al., 2017; Yoder et al., 2015; Yoder and Taube, 2011). The different target-specific presubicular projection neurons are well positioned to integrate anterior thalamic and retrosplenial inputs, but technical constraints have limited understanding of how known anatomical inputs are transformed into functional integrated output signals.

This work was therefore designed to examine the convergence of visual landmark information, that is possibly integrated in the RSC, and vestibular based thalamic head direction signals, in the PrS. Retrograde tracing was used to confirm inputs to the PrS from the ATN and the RSC. The spatial distribution of ATN and RSC targets in the dorsal and ventral PrS was investigated by stereotaxic injection of viral vectors inducing anterograde expression of light-gated ion channels fused to fluorescent reporters. We found that superficial layers of the dorsal PrS are major targets of ATN and RSC projections. We analyzed functional convergence of these inputs in the PrS using dual-wavelength optogenetic stimulations in ex vivo brain slices, while recording from layer 3 and 4 pyramidal neurons. Both ATN and RSC projections made mono-synaptic excitatory connections with single layer 3 principal cells and mostly di-synaptic ones with layer 4 cells. We show that EPSPs induced with close to coincident timing by ATN and RSC fibers summed non-linearly in layer 3 neurons. Layer 4 cell firing is facilitated by cholinergic activation. These data provide insights into the integration of landmark and head direction inputs and their distribution to downstream targets by PrS pyramidal cells.

Results

ATN and RSC send strong axonal projections to the dorsal Presubiculum

The origins of the main afferents projecting to the presubiculum were explored by injecting retrogradely transported fluorescent beads into the PrS (Figure 1A). After 4 days, coronal slices were prepared to examine the injection site and transport of the beads. Some beads remained close to the PrS injection site, due in part to local projections. Strong bead signals were detected within two of the subnuclei that form the anterior thalamus, the anterodorsal (AD) and anteroventral (AV) part of ATN. Neurons in AD were labeled most strongly in the medial portion of the AD, while labeled neurons in AV were found in its lateral portion (Figure 1B). Many neurons in the RSC were labeled. Cells with somata in layers 2 and 5 of the dysgranular dRSC were labeled, while mostly layer 5 cells of granular gRSC contained beads (Figure 1C). Regions adjacent to the presubiculum including the subiculum (Sub), parasubiculum (PaS) and the medial and lateral entorhinal cortices (MEC, LEC) were labeled as was the contralateral PrS. Beads were also detected in the laterodorsal thalamic nucleus (LD). Figure 1—figure supplement 1 shows an example of a series of labeled coronal sections from one out of two mice, indicating some labeling also in the visual cortices, perirhinal cortex, the nucleus reuniens of the thalamus, the dorsolateral geniculate nucleus, and the claustrum. Some beads were observed in the CA1 region, which has not previously been reported. Potentially though, this labeling could derive from a bead leak into the nearby PaS which is innervated by CA1 (Van Groen et Wyss 1990a). In summary, the ATN and RSC are the major sources of afferents projecting to the presubiculum with lesser inputs from other sites.

Projections from the ATN or RSC to the presubiculum were explored by injecting at these sites an anterogradely transported viral construct which expressed the modified Channelrhodopsin Chronos fused to GFP (Figure 1D). After 4 weeks, horizontal slices were prepared to verify the ATN injection site. Chronos-GFP labeling was mostly confined to the ATN, occasionally extending to medial thalamic and reticular nuclei nearby, possibly as bundles of projecting fibers (Figure 1E). After injection at the RSC site, coronal sections (Figure 1F) showed strong expression in layer 5, especially deeper zones, and layer 6 of both

129 dysgranular and granular RSC, while labeled dendrites were evident in layer 1. Chronos-GFP
130 expression extended throughout the RSC, from -1.7 to -3.7 posterior to Bregma on the
131 antero-posterior axis.
132 Projections of the ATN to the presubiculum were examined in horizontal sections
133 (Figure 1G). ATN axons expressing the Chronos-GFP construct targeted layers 1 and 3 of the
134 presubiculum, mostly avoiding layer 2 (Simonnet et al., 2017; Nassar et al., 2018). Labeling
135 was precisely limited to the presubiculum with a sharp reduction of green fluorescence at
136 the posterior border with the parasubiculum, the anterior border with the subiculum and
137 the lateral border with deep layers. Axon terminals in layer 3 were not homogeneously
138 distributed. Patches of higher density were evident in deep layer 3 (Figure 1G, left panel) or
139 in the upper layer 3 (Figure 1G, forth panel, and Figure 1K). Along the dorso-ventral axis, ATN
140 axons projected from -2 to -4 mm ventral to Bregma. Fluorescence was not detected in
141 adjacent regions including the Sub, PaS, and DG. ATN axons avoided layer 2 of the PrS,
142 including regions with patches of calbindin positive neurons that project to contralateral PrS
143 (Preston-Ferrer et al. 2016; Figure 1K).
144 RSC projections to the presubiculum (Figure 1H), traced with the fluorescent
145 Chronos-GFP construct, also projected to layers 1 and 3. Unlike ATN axons, they were
146 restricted to dorsal regions of the presubiculum (from -2 to -3 mm ventrally to Bregma on
147 the dorso-ventral axis; Figure 1H, I, J). RSC axons also presented a patchy innervation pattern
148 in L1-3, and tended to avoid microdomains of high-density ATN projections (Figure 1G, K.
149 Figure 3B). Overall, these data show ATN and RSC afferents innervate overlapping dorsal
150 regions of the PrS, in layer 1 and parts of layer 3. Different spatial patterns of fiber
151 terminations suggest distinct local connectivities.
152
153 **Layer 3 neurons are directly excited by both ATN and RSC afferents**
154 We next examined physiological effects of ATN and RSC afferents on PrS pyramidal
155 cells (Rees et al., 2017). Responses to photo-stimulation of the Chronos-GFP construct
156 injected either in the thalamus or in the retrosplenial cortex (Figure 2A) were recorded in
157 layer 3 neurons (Figure 2B). These cells had robust regular firing patterns in response to
158 depolarizing current injections (Figure 2C). Intrinsic properties of layer 3 cells were rather
159 uniform (Figure 2—figure supplement 1) and an unsupervised cluster analysis suggested
160 they formed a single population (Figure 2D).
161 Blue light activation of either ATN or RSC axons expressing Chronos-GFP reliably
162 evoked synaptic responses in whole-cell patch-clamp records from layer 3 cells. High
163 intensity stimulation (1 - 3 mW) evoked EPSCs or EPSPs with a probability of 84% (70/83
164 neurons from 14 mice) for ATN fibers and 85% (104/123 neurons from 20 mice) for RSC
165 fibers (Figure 2E). Excitatory postsynaptic currents or potentials evoked by optical
166 stimulation of thalamic and retrosplenial inputs will be referred to as oEPSCs and oEPSPs.
167 Mean oEPSC amplitudes (Figure 2F) were similar for ATN (-305.0 ± 61.0 pA, n = 24) and RSC
168 fiber stimuli (-305.8 ± 59.1 pA, n = 27). Response latency (Figure 2G) to ATN axon stimulation
169 was 2.45 ± 0.19 ms (n = 24) and that for RSC axon stimulation was 2.93 ± 0.23 ms (n = 27).
170 The variability in latency of oEPSCs (Figure 2—figure supplement 2A, B) induced by RSC
171 afferent stimuli was 0.35 ± 0.09 ms (n = 27) and that for oEPSCs induced by ATN stimuli was
172 0.19 ± 0.06 ms (n = 24). These short oEPSC latencies suggest monosynaptic transmission. We
173 confirmed this point by showing that oEPSCs were maintained in presence of TTX (1µM) and
174 4AP (100µM) (Figure 2H, n = 2 and 12 for ATN and RSC respectively). EPSCs induced by
175 stimulation of ATN and RSC fibers were reduced in amplitude and decayed more quickly in

176 the presence of the NMDA receptor antagonist APV (50 µM) and were completely abolished
177 by further application of the AMPA receptor antagonist NBQX (1 mM) (Figure 2I). The shape
178 of oEPSCs induced by light stimulation of ATN and RSC fibers was comparable. Rise times
179 were 1.38 ± 0.15 ms for ATN EPSCs (n = 15) and 1.38 ± 0.08 ms for RSC-mediated EPSCs (n =
180 15) and mean half-widths were 4.00 ± 1.02 ms for ATN-induced ESPCs (n = 15) and 4.34 ±
181 1.18 ms for RSC EPSCs (n = 15). The mean time constant (tau decay) for ATN-mediated EPSCs
182 was 3.01 ± 0.21 (n = 15) and for RSC-induced EPSCs 3.17 ± 0.27 (n = 15) (Figure 2—figure
183 supplement 2C-E.).
184 Optical stimulation of ATN and RSC fibers at lower light intensities elicited sub-
185 threshold synaptic events in layer 3 cells. oEPSP amplitude for ATN mediated events was
186 4.09 ± 1.18 mV (n = 11) and for RSC events it was 4.80 ± 0.84 mV (n = 11). Maximal rising
187 slopes were 2.93 ± 0.82 mV/ms for ATN-mediated events (n = 11) and 3.02 ± 0.53 mV/ms for
188 RSC EPSPs (n = 11), and decay time constants were 81.4 ± 11.6 ms for ATN EPSPs (n = 11) and
189 86.9 ± 11.2 ms for RSC EPSPs (n = 11). Rise times were shorter for subthreshold EPSPs
190 induced by ATN afferents at 3.00 ± 0.24 ms (n = 11) while those for RSC initiated EPSPs were
191 3.59 ± 0.34 (n = 11, p = 0.042, Wilcoxon test; Figure 2—figure supplement 2F-J). These data
192 show that ATN and RSC axons make monosynaptic, glutamatergic excitatory contacts on
193 layer 3 PrS cells.
194 The dynamics of responses to repetitive stimulation of layer 3 PrS cells were tested
195 using 20 Hz trains of light stimuli to activate either ATN or RSC afferents. oEPSCs for both
196 inputs followed depressing kinetics. Amplitude decreased for both inputs (Figure 2J, K),
197 significantly after the fourth pulse (Friedman's test and Dunn's multiple comparison test).
198 The *10/1* ratio was significantly lower than the paired-pulse ratio (PPR) in both cases (ATN
199 *10/1* 0.56 ± 0.05 vs PPR 0.86 ± 0.05, n = 15, p < 0.0001, Wilcoxon test, RSC *10/1* 0.64 ± 0.05
200 vs PPR 0.83 ± 0.03, n = 15, Wilcoxon test) (Fig 2L). ATN fiber stimulation induced PrS cell
201 firing in current-clamp with a high probability for initial stimuli and lower stable probabilities
202 for later stimuli in the train. Similarly, 20 Hz stimulation of RSC afferents evoked spikes with
203 high probability for initial stimuli and decreasing probabilities for later stimuli (on fourth and
204 7th-10th pulses, Friedman's and Dunn's multiple comparison tests; Figure 2M, N). Responses
205 to repeated subthreshold stimuli had similar dynamics (Figure 2O). Stimulation with lower
206 light intensities (< 1 mW) to initiate sub-threshold oEPSPs elicited different dynamic
207 responses. ATN afferent trains elicited responses with depressing dynamics: the amplitude
208 of the fifth oEPSP was significantly less than the first one (3.18 ± 0.88 vs 5.11 ± 1.64 mV, p =
209 0.0185, Friedman's and Dunn's tests). In contrast, subthreshold 20 Hz stimulation of RSC
210 afferents evoked little or no oEPSP depression (Figure 2—figure supplement 2K-M). These
211 data reveal distinct patterns of integration of repetitive activity in glutamatergic ATN and RSC
212 afferents terminating on PrS layer 3 pyramidal cells.
213
214 **Convergence of ATN and RSC inputs on single layer 3 neurons**
215 Are single layer 3 pyramidal cells innervated by both ATN and RSC afferents? It
216 seemed likely since the probability of connection to a given cell was 84% for ATN fibers and
217 85% for RSC afferents, and cluster analysis (Figure 2D) provided no evidence for
218 subpopulations of layer 3 cells in terms of intrinsic electrophysiological properties (see also
219 Balsamo et al., 2022).
220 We tested the hypothesis using photostimulation at two different light frequencies to
221 activate ATN and RSC afferents independently. However this approach may be compromised
222 since there is an overlap in the excitation spectra of blue-light activated Chronos (400-600

223 nm) and red-light activated Chrimson (450-700 nm; Klapoetke et al., 2014). Excitation of
224 Chronos with high intensities of blue light might also excite Chrimson. Stimulating with red
225 light at 630 nm should elicit neurotransmitter release in Chrimson-containing but not
226 Chronos-expressing fibers, which we found was indeed the case. Blue light stimuli at 470 nm
227 and intensities higher than 0.01 mW elicited oEPSPs in layer 3 cells of animals with Chronos-
228 expressing fibers. In contrast, blue light intensities higher than 0.25 mW were needed to
229 induce oEPSPs in different animals with Chrimson-expressing axons (Figure 3—figure
230 supplement 1A-D). Moreover, the amplitude of these events was smaller in Chrimson-
231 injected than in Chronos-injected mice. Thus, in our experimental conditions, blue light
232 intensities up to 0.25 mW could be used to excite Chronos-positive axons with confidence
233 that Chrimson-expressing fibers would not be stimulated.
234 We also tested the inverse, red light component of the dual stimulus strategy.
235 Intensities were tested in mice injected either with AAV5-Chronos to label ATN fibers or
236 AAV5-Chrimson to label RSC afferents. The strategy was validated by showing that red light
237 induced oEPSPs in Chrimson-containing, but not Chronos-expressing fibers, while blue light
238 evoked synaptic events in Chronos-, but not Chrimson-expressing fibers (Figure 3—figure
239 supplement 1E-K).
240 Injection in the same animal of the Chronos construction to the thalamus and that
241 for Chrimson to the retrosplenial cortex let us visualize ATN and RSC afferents to the
242 presubiculum (Figure 3A, B). Axon terminal fields of ATN and RSC projections were evident in
243 superficial layers of dorsal PrS (cf. Figure 1). Layer specificities, and labeling inhomogeneities
244 were apparent as were high density ATN patches below layer 2 with no RSC axon innervation
245 (Figure 3B). Layer 3 pyramidal cells could be innervated by ATN and RSC contacts both with
246 apical dendrites in layer 1 and basilar dendrites of layer 3 (Figure 3D). We found optical
247 stimulation of ATN and RSC axons, evoked synaptic responses in 14 out of 17 layer 3
248 pyramidal cells tested (current-clamp and voltage-clamp; Figure 3E, F).
249 In order to quantify substrates of these innervations, we counted numbers of labeled
250 ATN or RSC terminals located at less than 1µm from dendrites of biocytin filled layer 3
251 pyramidal cells (n = 6; Figure 3G). The distribution of these potential contact sites on
252 dendritic trees of layer 3 neurons was diverse. Some neurons exhibited highly segregated
253 domains receiving either ATN or RSC inputs. For instance, cell 1 had a high proportion of
254 clustered RSC putative synapses on its apical tuft while basilar dendrites were mostly
255 surrounded by potential thalamic terminals. In cell 2, RSC terminals were clustered close to
256 apical dendrites and also together with ATN terminals close to basilar dendrites. In contrast,
257 many ATN terminals were located closer to apical dendrites of cell 3. Segregation of cortical
258 RSC inputs to apical dendrites and thalamic ATN inputs to basal dendrites might favor
259 supralinear EPSP summation. However, afferent terminal distributions differed and we found
260 no clear pattern of sub- or supralinear summation (cell 1, supralinear summation
261 (Dual/summed EPSP, 1.39); cell 2, roughly linear (0.91); cell 3, sublinear (0.69), Figure 3G, H).
262 Furthermore, we noted certain potential contacts were located with separations less than 20
263 µm on the same dendrite (Figure 3I). Such proximity might underly local dendritic
264 computations and supra-linearities such as NMDA-mediated dendritic spikes which are
265 suggested to contribute to non-linear summation of synaptic events (Larkum et al., 1999,
266 2007, 2009).
267

Supralinear integration and amplification of ATN and RSC excitatory postsynaptic potentials

We explored interactions between excitatory inputs to layer 3 neurons by stimulating ATN and RSC axons separately with blue or red light. Excitatory synaptic potentials evoked by ATN or RSC axon stimulation, were compared to responses elicited when both sets of axons were activated at short time intervals (dual; Figure 4A). The mean amplitude of dual oEPSPs (synchronous light onset, Figure 4A-C) was significantly larger than calculated summed amplitudes of single oEPSPs (n = 11 cells, dual/summed amplitude 2.06 ± 0.55 mV, p = 0.0068, Wilcoxon test). Charge transfer, quantified as the surface under the dual oEPSP, was greater than the summed values for single oEPSPs (Dual/summed surface 2.21 ± 0.54 mV.s, n = 11, p = 0.0098, Wilcoxon test). These mean values cover variability between individual neurons. Summation of responses to ATN and RSC axon stimuli was supralinear in 7 out of 11 cells tested, linear for 3 cells and sublinear for 1 cell.

Dynamic responses to repetitive stimulations were also transformed by dual photostimulation. Amplitudes of 5 dual oEPSPs elicited at 20 Hz were higher than for a linear summation (Amplitudes in mV, Summed vs. Dual: Stim 1, 7.7 ± 1.9 vs. 11.1 ± 1.9; Stim 2, 6.7 ± 1.6 vs. 9.5 ± 1.5; Stim 3, 6.5 ± 1.4 vs. 9.5 ± 1.5; Stim 4, 6.1 ± 1.3 vs. 9.2 ± 1.5; Stim 5, 5.9 ± 1.3 vs. 8.6 ± 1.4, p = 0.0117, Two-way ANOVA; Figure 4E) and charge transfer, quantified as the surface under the 5 oEPSPs, also typically summed supralinearly (20 Hz, Surface in mV.s, Summed vs. Dual: Stim 1, 136.9 ± 30.6 vs. 221.2 ± 41.5; Stim 2, 143.3 ± 25.7 vs. 242 ± 43.9; Stim 3, 147.3 ± 22.5 vs. 259.2 ± 44; Stim 4, 145.1 ± 22 vs. 263.5 ± 49.2; Stim 5, 145.6 ± 23.2 vs. 258.7 ± 45.2, p = 0.0128, Two-way ANOVA; Figure 4F). Trains of dual ATN and RSC fiber stimulations also showed increased oEPSP integrals, compared to the stimulation of either one set of fibers alone, indicating stronger excitation over time (Figure 4E, F). Taken together, these data show supralinear summation of ATN and RSC inputs in most single layer 3 pyramidal cells, and also a facilitation of dynamic responses to repetitive inputs at 20 Hz.

We next asked how efficiently action potentials were induced by combined ATN and RSC inputs. Firing probability of layer 3 cells was higher for dual than for single input stimulation at a membrane potential of -65 mV (ATN 0.008 vs Dual 0.268, n = 5, p = 0.0216, RSC 0.024 vs Dual 0.268, n = 5, p = 0.1195, Friedman's and Dunn's tests) and higher still at -55 mV (Figure 4G, H). Firing was induced over a narrow window of time delays between stimulation of the two inputs (Figure 4I, J). It occurred for delays of -2 to +5 ms (RSC preceding ATN stimulus) reaching a maximum at a delay of +1 ms.

Supralinear summed responses of excitatory synaptic events may be mediated via the activation of NMDA receptors or voltage dependent intrinsic currents that amplify EPSPs (Fricker and Miles, 2000), especially if synaptic inhibition is reduced. We assessed these mechanisms in records made from layer 3 pyramidal neurons using a Cesium-based internal solution to favor cationic amplifying currents, and also containing QX314 to suppress action potentials (Figure 5). In 3 cells (from 2 mice) photostimulation of ATN fibers evoked oEPSPs of amplitude 10.9 ± 2.0 mV and RSC fiber stimulation induced events of 13.7 ± 2.5 mV. The response dynamics to 5 light pulses at 20 Hz were moderately facilitating (2nd vs 1st amplitude ratio: ATN 1.39, RSC 1.17; 5th vs 1st: ATN 1.18, RSC 1.20; n = 3). Coincident activation of ATN and RSC afferents induced supralinear oEPSP summation. Furthermore, repetitive stimulation generated large all-or-none depolarizations on the second or third stimulus at 20 Hz (2nd vs 1st amplitude ratio: 1.52; 5th vs 1st: 2.90; n = 3 cells, Figure 5A). It may be mediated by VGCC or a QX-314 resistant Na+ inward current (Fricker et al., 2009). This component appeared with higher probability and shorter latency in the presence of

315 $GABA_A$ receptor blocker gabazine (Figure 5B). The NMDA receptor antagonist APV largely
316 abolished the dual EPSP amplification initially (Figure 5C, black trace; 2nd vs 1st integral
317 ratio: 1.22; 5th vs 1st: 1.32), although amplification was partially restored by increasing RSC
318 stimulus intensity (pale pink trace; "amplification" refers to the shape of the plateau-like
319 prolongation of the peak, most pronounced on the second EPSP, indicated with an arrow).
320 NMDA receptor activation thus assists depolarization towards the threshold of a voltage-
321 dependent process contributing to supra-linear EPSP summation, but is not the only charge
322 carrier involved.
323
324 **Cholinergic modulation and recruitment of presubicular layer 4 neurons by ATN and RSC**
325 **afferents**
326 Presubicular layer 4 neurons are intrinsic bursting pyramidal neurons that project to
327 the lateral mammillary nucleus (Huang et al., 2017). This pathway is critical for the
328 coordinated stable landmark control of HD cells in the thalamus and throughout the HD cell
329 circuit (Yoder et al., 2015; Yoder et al., 2017) To investigate the input connectivity of layer 4
330 principal cells, we recorded responses of these neurons to stimulation of ATN and RSC
331 afferents.
332 Layer 4 neurons labeled by retrograde tracers injected in the lateral mammillary
333 nucleus were located in the *lamina dissecans* of the presubiculum, below layer 3, where
334 thalamic axons ramify (Figure 6A-D). At the proximal end of the presubiculum, and in its
335 continuity (Ishihara and Fukuda 2016), some subicular neurons projecting to the medial
336 portion of the mammillary bodies are also labeled (Figure 6B). The apical dendrites of layer 4
337 presubicular neurons extended towards presubicular layer 1 as previously described (Huang
338 et al., 2017), but tended to circumvent layer 3 and avoid thalamic afferents, by swerving
339 towards the subiculum. Apical dendrites of some neurons crossed layer 3 obliquely, while
340 others avoided thalamic afferents in layer 3 (Figure 6C, D, Figure 6—figure supplement 1).
341 Layer 4 neurons had a more depolarized resting membrane potential, lower input
342 resistance and time constant than layer 3 neurons (Figure 6—figure supplement 2 compares
343 active and passive properties). A characteristic voltage sag in responses to hyperpolarizing
344 steps, indicated the presence of an I_h current. Layer 4 neurons discharged bursts of two or
345 three action potentials at the onset of a depolarizing step current injection and also after the
346 offset of hyperpolarizing steps (Figure 6E). These bursts were abolished by the T-type Ca^{2+}
347 channel blocker TTA-P2 (Figure 6F).
348 We next recorded responses of layer 4 neurons to optical activation of ATN or RSC
349 afferents together with effects of the same stimuli on layer 3 pyramidal cells (Figure 6G).
350 Overall, latencies of oEPSCs in layer 4 neurons were longer than for layer 3 (ATN layer 4, 6.2
351 ± 0.6 ms, n = 8, vs. layer 3, 2.4 ± 0.2 ms, n = 24; RSC layer 4, 5.6 ± 0.4 ms, n = 9, vs. layer 3,
352 2.9 ± 0.2 ms, n = 27; Figure 6H), indicating possible polysynaptic excitation of layer 4
353 neurons. Bath application of TTX-4AP did not abolish oEPSPs entirely, leaving a low
354 amplitude component with short, potentially monosynaptic latencies (latency ATN 3.9 ± 0.6
355 ms, RSC 2.9 ± 0.2 ms, n = 5; Figure 6I).
356 Comparison of the timing of synaptic events and firing (Fig 7A-C) showed that oEPSP
357 onset in layer 4 neurons occurred after firing in the layer 3 neuron, following ATN afferent
358 stimuli, in 4 out of 5 cell pairs. We also observed this sequence when RSC input was
359 activated, in one tested pair. Depolarization of the layer 3 cell via the patch pipette, initiated
360 firing, but EPSPs were not elicited in any simultaneously recorded layer 4 neuron (0 out of six
361 cell pairs tested). These data suggest that excitation of layer 3 cells by ATN and likely by RSC

afferents is transmitted to layer 4 neurons, even in the absence of direct evidence for mono-synaptic coupling between cell pairs.

In records from pairs of layer 3 and 4 neurons (n = 3; Figure 7D, E) layer 3 cells responded with precisely timed action potentials to low intensity stimulation of ATN afferents, while only very small oEPSPs were initiated in layer 4 neurons. Increasing the excitatory drive by stimulating RSC afferents elicited larger oEPSPs more reliably in layer 4 neurons. Higher intensity stimulation of both ATN and RSC axons, could evoke bursts of action potentials, with the activation of an underlying Ca^{2+} current in layer 4 cells (Figure 7E). We hypothesize that increasing the activity of layer 3 neurons by strong (and non-specific) stimulation of ATN and RSC afferents is needed to induce discharges in layer 4 cells. We should also note that strong photostimulation of a single set of afferent fibers could initiate discharges in layer 4 pyramidal cells, as was shown in records from mice where only one afferent brain area, ATN or RSC, expressed an opsin (Figure 7—figure supplement 1).

Overall, it seems probable that layer 3 neurons relay activity projected by ATN and RSC inputs onto layer 4 pyramidal neurons. However, evidence on this point could be improved. In n = 9 paired recordings, we did not detect functional synapses between layer 3 and layer 4 neurons. Anatomically, putative synaptic contacts between filled axons of layer 3 and dendrites of layer 4 cells, were not evident (n = 5 filled layer 4 cells; see also Peng et al., 2017). We did find a possible synaptic connection between two neighboring L4 neurons in one case (Figure 6—figure supplement 1D), with a close apposition between axon and dendrite. Recurrent excitation may promote bursting in a positive feedback loop in layer 4 neurons, and NMDA receptor related EPSP amplification favors burst firing (Figure 7F).

Neuromodulatory factors may help drive layer 4 cells to fire action potentials. As Presubiculum is rich in acetylcholinesterase (Slomianka and Geneser 1991), we examined excitability changes in the presence of a broad cholinergic agonist. The application of Carbachol (10 µM; Figure 7G) led to a depolarization of the recorded layer 4 neurons' membrane potential by 13 ± 4 mV, with increased action potential firing during a positive step current injection, and from the baseline (Figure 7Gi,ii).

Discussion

Understanding the anchoring of HD signals to environmental landmarks provides a useful framework to ask how external information is integrated to revise and improve brain representations. Here we show that thalamic ATN afferents signaling HD data and cortical RSC projections that carry landmark information converge on layer 3 pyramidal cells of the dorsal presubiculum. Independent optogenetic stimulation of these two glutamatergic afferents in slices was used to define mechanisms of their integration in the presubiculum. Most layer 3 cells were innervated by both ATN and RSC fibers, sometimes close on the same dendritic branches, sometimes on different dendrites. Nearly coincident EPSPs (2-5 ms) induced independently by ATN and RSC afferents, evoked non-linear membrane responses to trigger layer 3 cell firing, transmitted to the MEC. In a second processing step, layer 3 neurons also excite layer 4 pyramidal cells which receive little direct ATN and RSC innervation. These burst firing neurons may project a distinct, di-synaptically mediated, visually-updated HD signal to the LMN. Our data thus suggest that the dorsal presubiculum

integrates HD and landmark signals producing two distinct output signals which are transmitted to different regions. Cholinergic modulation may facilitate responses to salient stimuli, for flexible anchoring to landmarks.

Anatomical convergence of ATN and RSC projections in the dorsal Presubiculum

Retrograde tracing in this study confirmed strong projections to the presubiculum from the ATN and the RSC to the presubiculum (Figure 1). Anterior thalamic fibers (Van Groen et Wyss 1990c; 1990a; 1990b; 1992; Shibata et Honda 2012; Vogt et Miller 1983) ramify in and delimit the anatomical borders of the presubiculum (Liu et al., 2021; Simonnet et al., 2017). HD signals from HD cells of the anterior thalamus project to the presubiculum (Goodridge and Taube, 1997) where they form synapses directly with layer 3 pyramidal cells (Nassar et al., 2018). The retrosplenial cortex was the most strongly labeled cortical region innervating the presubiculum. We detected retrogradely transported beads in cells of layers 2 and 5 of dysgranular RSC, and layer 5 of the granular RSC across its antero-posterior axis (Sugar and Witter, 2016).

We examined the anatomy and physiology of these two afferent systems to ask how visual landmark signals from the RSC are combined with HD signals relayed via the ATN. Anterograde fiber tracing, with an AAV5 construct expressing Chronos-GFP, confirmed that axons from both regions project to superficial layers of the dorsal presubiculum. No RSC projections were found in ventral PrS for injections in rostral RSC, as previously noted (Jones and Witter 2007; Kononenko and Witter 2012). Both RSC and ATN innervated superficial presubicular layers 1 and 3, while sparing layer 2 containing somata of calbindin positive neurons (Figure 1K and cf. Balsamo et al. 2022). We detected microzones containing a high density of ATN-positive fibers, but no RSC fibers, in upper layer 3. It remains to be shown how these anatomical inhomogeneities may translate to functional modularity.

Pathway specific functional connectivity onto PrS layer 3 neurons.

Photostimulation of GFP-Chronos expressing axons let us compare synaptic events initiated in layer 3 pyramidal cells by fibers from the ATN or the RSC in dorsal presubiculum slices (Figure 2). Both ATN and RSC afferents formed mono-synaptic glutamatergic connections with components mediated by NMDA and AMPA receptors. The amplitudes of synaptic currents varied between neurons, with an overall similar amplitude distribution for ATN and RSC stimulation. This may be due to variable expression levels (Hooks et al. 2015), or may imply variations in coupling weights across cells. ATN and RSC fiber mediated EPSCs depressed during repetitive activation at 20 Hz. EPSPs induced firing early during repetitive stimulation. RSC inputs tended to produce more sustained EPSP dynamics and slower rise times than ATN afferents for low intensity stimulation. ATN synapses with presubicular pyramidal cells resemble those made by thalamic afferents in the somatosensory cortex - high release with depressing dynamics, (Gil et al., 1999) possibly due to presynaptic expression of VGLut2 (Liu et al., 2021).

Dual wavelength optogenetic stimulation was used for independent activation of intermingled afferents expressing blue-light sensitive Chronos in ATN fibers and red-shifted Chrimson in RSC fibers (Klapoetke et al., 2014). Precautions were taken to avoid cross-stimulation since all channelrhodopsin variants are somewhat sensitive to blue light. With the fast, sensitive opsin Chronos expressed in ATN fibers, synaptic events were induced by very short (0.5 ms), low intensity, 0.25 mW, stimuli. For RSC fibers expressing Chrimson, using light stimuli of duration 2 ms, adjusting intensity up to 2 mW initiated synaptic events

of comparable amplitude. Calibration experiments (Figure 3—figure supplement 1) provided strong evidence for the independence of responses. While Chrimson has slower dynamics than Chronos (Klapoetke et al., 2014), synaptic events induced by stimulating either opsin were similar, as we showed by swapping the two opsin variants injected in ATN and RSC fibers respectively (Figure 4).

This dual opsin approach permitted independent stimulation with blue and red light pulses. Most (76%) recorded layer 3 neurons generated synaptic events in response to stimulation of both ATN and RSC fibers providing a substrate for integration of landmark information from the RSC with thalamic HD signals. Layer 3 cell firing was most effectively triggered by nearly coincident inputs (-2 to +5 ms separation, Figure 4I, J). This is of interest since HD representations in the AD and RSC are highly coherent (Fallahnezhad et al., 2023), with short intervals between spikes in these two regions (< 5ms; van der Goes et al. 2022). Converging inputs from thalamic and retrosplenial axons can therefore excite common postsynaptic presubicular layer 3 neurons with very short delays, such that coincidence detection by these cells will tend to enhance HD signals. Response dynamics to combined stimulation of both inputs at 20 Hz were maintained or facilitating, in contrast to the depressing dynamics of repetitive stimulation of one set of afferent fibers. Combined and temporally precise inputs from ATN and RSC may thus help maintain HD signaling during immobility. Our findings may well underlie the recent in vivo observation by Siegenthaler et al (2024) that visual objects refine HD coding, and that presubicular HD cells whose preferred firing direction corresponds to a visual landmark respond with higher firing rates.

Nonlinear signal integration in layer 3 thalamo-recipient neurons and physiological significance for HD-to-landmark anchoring

Convergence of ATN and RSC axons onto single layer 3 pyramidal cells provides the anatomical basis of synaptic integration. Putative synaptic contacts from both afferent fiber systems were found on the basal dendrites of pyramidal cells (Figure 3), sometimes on the same branch. Photostimulation centered on the soma of recorded neurons predominantly activated synapses on basal dendrites. Supralinear summation could result from local spike-generating mechanisms if the activated synapses were located on a same dendritic branch (Makarov et al., 2023; Poirazi and Papoutsi, 2020; Polsky et al., 2004). Clustered synapses could also guide the formation of new spines and synapses during integration of landmark information in the HD signal. Learning might bind new inputs into functional synaptic clusters (Hedrick et al., 2022). Our small sample of layer 3 pyramidal cells suggest that both ATN and RSC axons target basal dendrites, and more RSC than ATN axons contact apical dendrites (Figure 3). Tests on the effects of precise, near coincident activation of basal and apical synapses could be revealing but were not technically possible in this study. Distinct dendritic inputs to layer 3 cells may improve spatial perception (Takahashi et al., 2016) enhancing HD signal quality by integration with landmark information.

Our data show that EPSPs elicited by nearly coincident ATN and RSC inputs which exceed a threshold are amplified by NMDA receptor activation and voltage gated inward dendritic currents (Figure 5; Fricker et al. 2009). From a small sample of cells it appears that EPSP amplification may be facilitated by a reduction in synaptic inhibition (n = 3; Figure 5), indicating that disinhibition may be permissive for supralinearity and gate firing by dynamic modulation of the balance between inhibition and excitation (Milstein et al., 2015). VIP expressing interneurons, which are excited by cholinergic modulation could provide such disinhibition of the presubicular microcircuit (Porter et al., 1999; Slomianka and Geneser,

1991). The excitation-inhibition balance in pyramidal cells may become tipped towards excitation in the case of coincident, co-tuned thalamic and retrosplenial input. A 'when-to-learn' signal for HD updating in the presubiculum might function analogously to the promotion by dopamine of associations between sensory cues and head direction cells in the fly (Fisher et al., 2022). It is however unclear whether LTP type learning takes place in the mammalian head direction circuit. Presubicular layer 3 cells do not express the GluR1 subunit of AMPA receptors (Martin et al 1993; Ishihara et al., 2016) that is critical for LTP expression (Boehm et al., 2006). The absence of GluR1 might indicate that the thalamo-presubicular synapses in layer 3 function without classical long-term synaptic plasticity. Matching directional with visual landmark information based on temporal coincidence may be sufficient. Algorithms for dynamic control of cognitive maps without synaptic plasticity (Whittington et al 2025 Neuron) propose that working memory is stored in neural attractor activity, and updated by recurrent connections, which might generalize to the HD system.

Layer 3 pyramidal cells may be described as multi-compartmental computational devices (Häusser and Mel, 2003; Mel, 1993; Poirazi et al., 2003; Spruston, 2008) which integrate HD and landmark information. ATN axons drive presubicular HD neurons (Peyrache et al., 2015) and RSC mixed selectivity neurons contribute visual landmark information and allocentric spatial references (Jacob et al., 2017; Mitchell et al., 2018; Vann et al., 2009). NMDA mediated dendritic spikes enhance tuning selectivity in visual cortex (Smith et al., 2013; Wilson et al., 2016) and barrel cortex (Lavzin et al., 2012). Dendritic events in Layer 3 PrS cells may enable binding of visual landmarks with HD tuning. It is tempting to speculate that nonlinear synaptic integration and inhibitory gating may be involved in flexibly updating the allocentric direction of HD cells based on the integration of visual landmark information to the current HD signal (Siegenthaler et al., 2024). In the primary sensory cortex, nonlinearities act to increase perceptual threshold of sensory information (Takahashi et al., 2016; 2020). The attractor network in the PrS could thus be either stabilized or flexibly reset to external spatial cues.

Alternative models of HD-to-landmark anchoring have focused on the RSC, which also treats HD and landmark signals (Page & Jeffrey, 2018; Yan, Burgess, Bicanski, 2021). Possibly the RSC registers a direction to a landmark rather than comparing it with the current HD (Sit & Goard, 2023). The integrated information would then reach PrS, which in contrast to RSC, is uniquely positioned to update the signal in the LMN (Yoder et al., 2011).

What is the neuronal and circuit mechanism for integrating the "right" set of landmarks to anchor the HD signal? In our slice work we are blind to the exact nature of the signal that is carried by ATN and RSC axons. Critical missing information to understand the logic of HD-to-landmark anchoring also includes the degree of divergence and convergence of connections from a single thalamic or retrosplenial neuron. Do HD tuned inputs from thalamus converge on similarly tuned HD neurons only? Is divergence greater for the retrosplenial inputs? If so, thalamic input might pre-select a range of HD neurons, and converging RSC input might narrow down the precise HD neurons that become active (Figure 7—figure supplement 2). In the future, activity dependent labeling strategies might help to tie together information on the tuning of pre-synaptic neurons, and their convergence or divergence onto functionally defined postsynaptic target cells.

Functional significance of two-layer processing preceding projection to LMN

Burst-firing layer 4 PrS cells project a distinct version of HD-landmark signals to the LMN. The dendrites of these LMN projecting neurons overlap little with direct ATN and RSC

inputs granting partial isolation from direct excitation, and permitting a second level of integration of information from layer 3 neurons. Layer 3 axons may innervate layer 4 neurons basal dendrites, which may be driven to fire by sufficiently strong excitatory inputs from layer 3, especially if combined with cholinergic activation.

There are advantages to segregating the integration of converging input signals from the updating signal across layers. Segregation permits both a fast transmission of an integrated signal to the medial entorhinal cortex, and the conditional transmission of an updating signal mediated by burst firing to upstream HD circuit elements. The synaptic threshold implicit in this two-stage system permits a gated updating. Functionally layer 4 neurons are uniquely positioned to update the HD signal in the LMN with visual landmark information (Yoder et al., 2015). In this way, cell-type specific cholinergic facilitation may help idiothetic cue based navigation (Yoder et al., 2017). These cellular and synaptic circuit data support and expand the findings of Yoder et al. (2015 and 2017). They clarify how the thalamic HD signal integrated with visual landmark information is relayed to the grid cell system in the medial entorhinal cortex and to the lateral mammillary nuclei.

Limitations

Burst firing may play a role for learning in hierarchical circuits (Naud et al., 2023; Payeur et al., 2021). In the HD circuit, landmark information contained in bursts might reset or anchor the HD attractor in the LMN and beyond. The effects of burst firing signals transmitted to the LMN remain to be assessed. Potentially HD signals may be updated with visual signals at several sites including the PrS, but PrS uniquely provides a feed-back projection to the lateral mammillary nucleus. Further work on layer 3 to layer 4 transmission is warranted, and the link to spatial perception and behavioural updating needs to be strengthened.

Methods

Animals

Experiments were performed on male and female wild-type and transgenic (Ai14 reporter line - Jax n007914) C57Bl6 mice of age 35-70 days, housed on a 12-hours light/dark cycle with food and water available *ad libitum*. Animal care and use conformed to the European Community Council Directive (2010/63/EU) and French law (87/848). Our study was approved by the local ethics committee (CEEA - 34) and the French Ministry for Research 01025.02.

Viral vectors and beads

Projecting neurons were labeled with retrograde fluorescent tracers (Retrobeads, Lumafluor, and AAV2retro-CAG-tdTomato, Addgene 59462P). Fluorescent beads were stored at 4°C before use. Channelrhodopsin expression was achieved by injecting Adeno-associated viral constructions. AAV5.Syn.Chronos-GFP.WPRE.bGH (AAV5-Chronos, Penn Vector Core, Addgene 59170P) was used to induce neuronal expression of the blue light induced channelrhodopsin Chronos fused to the GFP marker and under the control of the Synapsin promoter. AAV5.Syn.ChrimsonR-tdTomato.WPRE.bGH (AAV5-Chrimson, Penn Vector Core, Addgene 59171P) induced neuronal expression of the red light gated channelrhodopsin Chrimson fused to the tdTomato marker, under the control of the Synapsin promoter. Viral

595 vectors were stored at -80°C before use.
596
597 **Stereotaxic surgery**
598 Mice at ages of 4-5 weeks were anesthetized by intraperitoneal (i.p.) injection of a
599 mixture of ketamine hydrochloride and xylazine (100 and 15 mg/kg respectively, in NaCl
600 0.9%). They were placed in a stereotaxic frame for injections. Fluorescent beads for
601 retrograde tracing were injected (300-500 nl) into the PrS at the coordinates: -4.06 antero-
602 posterior (AP), 2.00 medio-lateral (ML) and -2.15 mm dorso-ventral (DV) and into the LMN (-
603 2.8 AP, 0.75 ML, -5.35 DV) with respect to the bregma. Note, due to the small size of LMN,
604 some overflow to the medial mammillary nucleus (MMN) may have occurred.
605 Viral injections were performed unilaterally (Mathon et al., 2015; Richevaux et al., 2019) at
606 the coordinates -0.82 AP, 0.75 ML and -3.2 mm DV for the ADN, and at -2.1 to -2.15 AP, 0.65
607 ML and -0.65 mm DV for the RSC. Volumes of 200 to 250 nl were injected with a 10 µL
608 Hamilton syringe equipped with 33ga needle over a time of 10 min. The needle was slowly
609 removed after a delay of 10 min to avoid leakage from the injection site. Best expression of
610 AAV5 serotypes was achieved after 3 to 4 weeks.
611
612 **Tissue fixation and slicing for retrograde tracing**
613 Brains were removed for anatomy at 4 days after retrobead injection. Mice were
614 anesthetized by i.p. injection of the ketamine/xylazine mixture. An intracardiac perfusion
615 with 0.1M PBS was followed by perfusion with 4% paraformaldehyde. Brains were stored
616 overnight in paraformaldehyde at 4°C and then washed in PBS. Coronal or horizontal
617 sections were cut at 100 µm with a vibratome and stored in sucrose at 4°C.
618
619 **Preparation of brain slices for physiology**
620 Slices of the temporal lobe were prepared 3-4 weeks after injection of AAV5 viral
621 constructions. Mice were anesthetized by i.p. injection of the ketamine/xylazine mixture.
622 They were then perfused intracardially with a cutting solution containing (in mM): 125 NaCl,
623 25 sucrose, 2.5 KCl, 25 $NaHCO_3$, 1.25 NaH_2PO_4, 2.5 D-glucose, 0.1 $CaCl_2$, 7 $MgCl_2$, cooled to
624 4°C, and oxygenated with a 5% CO_2 / 95% O_2. The brain was removed and a vibratome was
625 used to cut horizontal slices at 300 µm in the same solution. Slices were stored for 15 min at
626 34°C in an ACSF containing (in mM): 124 NaCl, 2.5 KCl, 26 $NaHCO_3$, 1 NaH_2PO_4, 2 $CaCl_2$, 2
627 $MgCl_2$, and 11 D-glucose, bubbled with 5% CO_2 / 95% O_2. They were then kept in the same
628 solution at room temperature until recording.
629
630 **Whole-cell patch-clamp recordings**
631 Slices were transferred to a recording chamber perfused with oxygenated, warmed
632 (~32 °C) ACSF mounted on an epifluorescence microscope. Patch-clamp records were made
633 from neurons with borosilicate glass pipettes of external diameter 1.5 mm (Clark Capillary
634 Glass, Harvard Apparatus) pulled with a Brown-Flaming electrode puller (Sutter
635 Instruments). Electrodes, filled with a potassium-gluconate based solution containing (in
636 mM): 135 K-gluconate, 1.2 KCl, 10 HEPES, 0.2 EGTA, 2 $MgCl_2$, 4 MgATP, 0.4 Tris-GTP and 10
637 Na_2-phosphocreatine, had a resistance of 4-8 MΩ. An alternative, cesium-gluconate based
638 solution facilitated neuronal depolarization to examine synaptic inhibition, in Figure 5. It
639 contained (in mM): 125 Cs-gluconate, 10 HEPES, 0.2 EGTA, 2 $MgCl_2$, 4 MgATP, 0.4 Tris-GTP
640 and 10 Na_2-Phosphocreatine, together with 5 mM QX-314 to block Na^+ channels. Pipette
641 solutions also contained 3 mM biocytin to reveal morphology after recording. They were

642 adjusted to pH 7.3 and osmolarity 290 mOsm. Whole-cell, patch-clamp signals were filtered
643 at 3kHz, amplified with a MultiClamp 700B amplifier and acquired with pCLAMP software
644 (Molecular Devices). In a subset of experiments, the following drugs were used to modulate
645 the responses to optogenetic stimulations; the presence of these drugs is indicated in the
646 figure and figure legend, whenever applicable. Monosynaptic excitation induced by optical
647 stimulation was tested in the presence of TTX (1 µM) and 4-AP (100 µM). NBQX (10 µM) and
648 APV (100 µM) were used to block AMPA and NMDA receptors respectively. Gabazine (10
649 µM) was used to block $GABA_A$ receptors. Carbachol (10 µM) was used to activate
650 acetylcholine receptors. All drugs were bath applied.
651
652 **Optical stimulation**
653 LED illumination (Cairn Research, OptoLED) was used to visualize the fluorescent
654 reporters GFP and tdTomato, and to stimulate opsin-expressing axons, using a 470 nm LED
655 for Chronos and a 627 nm LED for Chrimson. Illuminated spots had a diameter of 200 µm
656 with a 60x objective and were centered on the recorded cell soma. Photostimulation thus
657 covered most of the basilar dendrites of layer 3 pyramidal neurons (typical distance from tip
658 of apical to tip of basilar dendrite <400µm). Stimuli consisted of light pulses of 0.5 to 5 ms
659 duration, repeated 5-10 times at 20 Hz.
660 A multiband filter allowed simultaneous stimulation by blue and red LEDs of axons
661 containing Chronos and Chrimson (Simonnet et al., 2021). Stimulus power intensity (set in
662 mV) was calibrated as light intensity. The response probability of layer 3 cells was calibrated
663 to blue or red illumination of ATN or RSC afferents expressing Chronos or Chrimson to avoid
664 stimulus overlap (Figure 3—figure supplement 1). Chronos was targeted to the ATN and
665 Chrimson to the RSC after testing the reverse configuration. Projections from the thalamus
666 are larger and Chronos is more sensitive to blue light, so this configuration assured reliable
667 activation of thalamic fibers at minimal blue-light intensities. For experiments investigating
668 the integration of ATN and RSC inputs, we aimed to give similar weights to both inputs:
669 Chrimson-expressing fibers were stimulated with light of intensity adjusted to initiate
670 optically evoked excitatory postsynaptic potentials (oEPSPs) of amplitude similar to those
671 induced by blue light Chronos-fiber stimuli.
672
673 **Data analysis**
674 ATN and RSC projections to the PrS, were analyzed from Chronos and Chrimson
675 expression, using the ImageJ Plot Profile plug-in to quantitate normalized plot profiles (2000
676 pixels) of horizontal presubicular sections. Dorso-ventral differences were derived by
677 dividing differences in labeling intensity between the PrS and the dentate gyrus (DG)
678 molecular layer by DG intensity in slices from 5 dorso-ventral PrS levels. Values from all
679 animals were averaged and then normalized.
680 Cells were qualified as synaptically 'connected' when they responded to light
681 stimulation of afferent axons with a delay < 8 ms. Slices with very low or absent expression
682 of the fluorescent reporter were excluded. Cells were qualified as 'non-connected'
683 synaptically, if they did not respond to light stimulation, but at least one neighboring cell in
684 the same slice did.
685 Intrinsic neuronal properties were analyzed with custom MATLAB routines to derive
686 15 electrophysiological parameters (Huang et al., 2017). Parameters were standardized and
687 unsupervised cluster analysis performed with MATLAB was used to compare different
688 neurons (Huang et al., 2017; Simonnet et al., 2013).

Axograph was used to analyze responses to optical stimulation of ATN and RSC fibers. Layer 3 neurons were recorded at potentials near -65 mV. Responses to light were averaged from 10 stimulus trains at 20 Hz. Amplitudes and latencies of initial light evoked EPSCs, of latency shorter than 10ms, were quantified from voltage-clamp records. Latency was measured from stimulus onset to 10% of the peak amplitude of the first optically induced EPSC. Amplitude was measured with respect to the pre-stimulus baseline. Paired-pulse ratio (PPR) was defined as the ratio of the amplitude of the second to the first EPSC and 10/1 ratio as that between the 10th and the 1st EPSC, in responses to 20 Hz stimulations. Spike probability was counted over 5 to 10 trials per cell and then averaged over all cells. EPSPs induced by dual wavelength stimulation were analyzed using Axograph and a custom-made software. Events evoked by light stimuli were detected in a window of 1-10 ms after stimulation. EPSP amplitude and integrated area were calculated over 50 ms after stimulation. Baseline suppression was applied using an average of membrane potential during 50 ms before stimulation. Summation of ATN and RSC evoked EPSCs in layer 3 neurons was determined from the amplitude and integral of averaged events. Summation was considered to be supralinear, if values were more than 10% higher than a linear addition, linear for values within ± 10%, and sublinear for values more than 10% lower.

Biocytin revelation and morphology

Recorded neurons were filled with biocytin to visualize their morphology and location. Slices were fixed in 4% PFA in 0.1 M PBS at 4°C overnight, washed 3 times in 0.1 PBS and cryoprotected in 30% sucrose. Cell membranes were permeabilized by three freeze-thaw cycles over dry ice and rinsed in PBS. Slices were agitated in a saturation buffer (2% milk, 1% Triton X-100 in 0.1 M PBS) for 2 hours at room temperature. They were then incubated with Streptavidin-Cy5 conjugate (1:500) and DAPI (1:1000) overnight at 4°C. Sections were washed 3 times with PBS and mounted on coverslips with ProLong gold antifade mountant. For anatomical study they were mounted in Mowiol medium. Cell, bead and virus expression were visualized with an epifluorescence microscope. Higher resolution of morphology was obtained with confocal microscopy. Cell morphologies were reconstructed using IMARIS.

Quantification and statistical analysis

Data was analyzed with AxoGraphX and custom-written software (MATLAB, The MathWorks). Results are given as mean ± SEM. Statistical analysis was performed with Prism (GraphPad Software). The Mann-Whitney unpaired t-test was used to compare two groups. The Wilcoxon or Kruskal-Wallis test was used to compare paired groups. Evolution of parameters evoked by optical stimulation (current or potential amplitudes, spike probability) was analyzed with Friedman's test followed by multiple comparison Dunn's test. Šidák's multiple comparison test was also used to compare linear and observed responses to ATN and RSC stimulations. Significance levels are given as p values.

Data availability

Data are available upon request to the corresponding authors Desdemona Fricker and Louis Richevaux. The Matlab code for analysis of intrinsic properties is available at *https://github.com/schoki0710/Intrinsic_Properties*.

Acknowledgements

This work is supported by the Centre National de la Recherche Scientifique and the Université Paris Cité. DF received funding from the Agence Nationale de la Recherche (ANR-DFG Program, ANR-18-CE92-0051 BURST), from the ERA-NET NEURON Program (ANR-20-NEUR-0005 VELOSO), and the FLAG-ERA HBP Program (ANR-21-HBPR-0002 VIPattract). This work has benefited from support by the BioMedTech Facilities at Université Paris Cité (Institut National de la Santé et de la Recherche Médicale Unité S36/Unité Mixte de Service 2009). We thank Dr. Li-Wen Huang for help with analysis routines. We thank Dr. Kate Jeffery and the Royal Society COST-share program, technical assistance from Fabrice Licata and Dr. Abdelali Jalil from the UPC Microscopy platform, Claire Lovo from ICM Quant, Dr. Boris Lamotte d'Incamps, and Dr. Richard Miles for helpful comments on the manuscript.

Author contributions

L.R. and D.F. conceived experiments, designed study, and interpreted data. D.F. acquired funding, L.R. and D.F. managed the project. L.R., D.L., M.N., C.M., L.D-R. and N.S-F. performed experiments and analyzed data, I.C. helped with analysis software, L.R. and D.L. prepared figures, L.R. and D.F. wrote the manuscript.

Declaration of Interests

The authors declare no competing financial interests.

Figure titles and legends

Figure 1 with 2 supplements.

ATN and RSC send strong axonal projections to the superficial layers of dorsal Presubiculum

A, Retrograde labeling of cortical and subcortical regions projecting to the presubiculum (PrS) with retrobeads.

B, Ipsilateral anterodorsal and anteroventral thalamic nuclei are labeled with beads.

C, Ipsilateral granular (gRSC) and dysgranular (dRSC) retrosplenial cortex labeling. Scale bars B, C, 200 µm.

D, Anterograde labeling of thalamic and retrosplenial projections to PrS with AAV-Chronos-GFP.

E, F, Injection sites in ATN (E) and RSC (F). AD: anterodorsal thalamic nucleus, AV: anteroventral thalamic nucleus, CA1: field of the hippocampus, cc: corpus callosum, cg: cingulum, CPu: caudate putamen, DG: dentate gyrus, MD: thalamic medial dorsal nucleus, MEC: medial entorhinal cortex, PaS: parasubiculum, PVA: paraventricular thalamic nucleus, anterior, Rt: thalamic reticular nucleus, sm: stria medullaris, Sub: subiculum, VL: thalamic ventrolateral nucleus.

G, H, Five sequential 100-µm horizontal slices of the parahippocampal region show ATN (G) and RSC (H) axons expressing Chronos-GFP (green). Dashed lines show limits of the parahippocampal region to the left and of the dentate gyrus to the right. Numbers show

779 dorsoventral level with respect to bregma. Scale bars 100 µm.
780 I, Normalized profiles of fluorescent intensity for ATN and RSC projections to the
781 presubiculum, from white matter (WM) to pia (PIA). Mean (green) ± SEM (grey), n = 8 slices
782 each.
783 J, Ventral (V) to dorsal (D) normalized distribution of ATN and RSC projections to the
784 presubiculum, n = 3 mice.
785 K, ATN axon labeling (green) is segregated from calbindin labeling (white) in the PrS. Scale
786 bar 100 µm.
787 See also Figure 1—figure supplement 1.
788
789 **Figure 1—figure supplement 1. Brain regions providing input to the Presubiculum.**
790 Semi-quantitative estimate of retrobeads labelling in serial coronal slices following injection
791 in the presubiculum. Color intensity represents beads density (mouse #69).
792 - Thalamic nuclei: anterodorsal (AD) +++, anteroventral (AV) +++, laterodorsal (LD)
793 +++, lateroposterior ++, dorsal lateral geniculate ++, reuniens ++, anteromedial -,
794 ventrolateral -
795 - Retrosplenial cortex: dysgranular (dRSC) +++, granular +++, dysgranular
796 contralateral ++
797 - Visual cortex: primary (V1) ++, secondary (V2L) +++
798 - Entorhinal cortex: lateral (LEnt) +++, medial (MEnt) +++
799 - Hippocampus/parahippocampus: parasubiculum (PaS) +++, subiculum (Sub) +++,
800 controlateral PrS ++, CA1 ++, CA3 -, dentate gyrus –
801 - Other: claustrum ++, perirhinal cortex ++, temporal association cortex ++
802
803 ADN: anterodorsal thalamic nucleus; AM: anteromedial thalamic nucleus; APT(V): anterior
804 pretectal nucleus (ventral part); AVDM: anteroventral thalamic nucleus, dorsomedial part;
805 AVVL: anteroventral thalamic nucleus, ventrolateral part; CA: cornu ammonis; cc: corpus
806 callosum; Cl: Claustrum; Cg1,2: cingular cortex area 1,2; coll. sup: colliculus superior; CPu:
807 caudate putamen (striatum); dhc: dorsal hippocampal commissure; DG: dentate gyrus; DLG:
808 dorsal lateral geniculate nucleus; LEnt: lateral entorhinal cortex; LDDM: laterodorsal thalamic
809 nucleus, dorsomedial part; LDVL: laterodorsal thalamic nucleus, ventrolateral part; LMN:
810 lateral mammillary nucleus; LS: lateral septal nucleus; M1,2: primary, secondary motor
811 cortex; MEnt: medial entorhinal cortex; MMN: medial mammillary nucleus; PAG:
812 periaqueductal gray; PaS: Parasubiculum; PF: parafascicular thalamic nucleus; PH: posterior
813 hypothalamic area; PMCo: posteromedial cortical amygdaloid nucleus; Po: posterior
814 thalamic nuclear group; PRh: perirhinal cortex; PrS: presubiculum; PVA: paraventricular
815 thalamic nucleus, anterior part; S1BF, S1FL, S1ULp, S1Tr: primary somatosensory cortex,
816 barrel field, forelimb region, upper lip region, trunk region; S2: secondary somatosensory
817 cortex; sm: stria medullaris of the thalamus; Sub: subiculum; Subst. Nigra: substantia nigra;
818 Re/Reuniens: reuniens thalamic nucleus; RSA = dRSC, dysgranular retrosplenial cortex; RSC:
819 retrosplenial cortex; RSG = gRSC: granular retrosplenial cortex; Rt: reticular thalamic nucleus;
820 V1: primary visual cortex; V2M: secondary visual cortex, medial part; V2L: secondary visual
821 cortex, lateral part; VA: ventral anterior thalamic nucleus; VDB: nucleus of the vertical limb
822 of the diagonal band; VL: ventrolateral thalamic nucleus; VPL: ventral posterolateral thalamic
823 nucleus; VPM: ventral posteromedial thalamic nucleus
824

825 **Figure 1 - Supplement 2. Calbindin immunostaining and GFP-expressing ATN axons in**
826 **horizontal sections.**
827 A, Subicular (Sub), Parasubicular (PaS), medial entorhinal cortical (MEC), and presubicular
828 (PrS) borders are outlined, as well as the dentate gyrus (DG). Patches of high density of ATN
829 axonal ramifications in L3 are indicated as "ATN microdomains".
830 B, Territories devoid of ATN axons in PrS L2 stain positive for calbindin.
831
832 **Figure 2** with 2 supplements.
833 **Responses of layer 3 presubicular cells to photoactivation of ATN and RSC fibers.**
834 A, Expression of AAV5-Chronos in ATN or RSC.
835 B, Biocytin labeled layer 3 cells (white) and GFP positive axons (green) from the ATN or RSC.
836 Scale bar 10 µm.
837 C, Firing pattern of two layer 3 cells receiving inputs from the ATN (*cerulean*) and the RSC
838 (*purple*). Insets show current commands.
839 D, Cluster analysis of physiological parameters for cells tested by stimulating ATN (n = 29
840 cells /14 mice) or RSC (n = 43 cells/20 mice) fibers.
841 E, Representative EPSCs evoked in layer 3 cells by light stimulation (blue bar) of ATN or RSC
842 inputs. Right, proportion of cells receiving ATN or RSC inputs.
843 F, Average amplitudes of ATN and RSC induced synaptic currents. Mann-Whitney U test
844 revealed no significant difference (p = 0.95).
845 G, Latency of EPSCs evoked by light-stimulation of ATN (n = 24 cells/12 mice) or RSC fibers (n
846 = 27 cells/14 mice). Mann-Whitney U test revealed no significant difference (p = 0.13).
847 H, EPSPs induced in layer 3 cells (single traces) by stimulating ATN or RSC inputs in absence
848 and presence of 1 µM TTX and 100 µM 4-AP.
849 I, EPSCs induced by stimulating ATN or RSC fibers in the absence and presence of 100 µM
850 APV and APV + 10 µM NBQX. Holding potential +40 mV.
851 J, Voltage-clamp responses of layer 3 cells to 20 Hz train stimulations of ATN (*left*) and RSC
852 (*right*) inputs. Insets show EPSCs in response to the first two stimuli.
853 K, oEPSC amplitudes for 10 ATN or RSC fiber stimuli at 20 Hz (ATN, n = 15 cells/8 mice, RSC, n
854 = 15 cells/11 mice). Short middle line, mean; Min to max and quartiles.
855 L, Paired-pulse ratio (PPR) and 10/1 ratio (ratio between 10th and 1st event amplitudes) for
856 ATN or RSC inputs. Wilcoxon matched-pairs signed rank test: ATN PPR vs 10/1 **** p <
857 0.0001, RSC PPR vs 10/1 *** p = 0.0001.
858 M, Current clamp traces showing action potentials and EPSPs evoked by 10 stimuli at 20 Hz.
859 N, Spiking probability during trains of 10 stimuli. ATN, n = 6 cells/4 mice, RSC, n = 12 cells/9
860 mice. Full line, median; short line, mean; Min to max and quartiles. In K and N, * p < 0.05, **
861 p < 0.01, *** p < 0.001, **** p < 0.0001 from Friedman's test followed by Dunn's *post-hoc*
862 test.
863 O, oEPSP amplitudes for trains of 5 stimuli at 20 Hz.
864 See also Figure 2—figure supplements 1 and 2.
865
866
867 **Figure 2—figure supplement 1. Table showing the intrinsic electrophysiological**
868 **physiological properties of layer 3 cells tested for responses to stimulating ATN or RSC**
869 **fibers.**
870

871 **Figure 2—figure supplement 2. Comparison of evoked synaptic events in presubicular layer**
872 **3 neurons following photostimulations of ATN or RSC axons.**
873 A, Variance of latency (jitter) in oEPSP onset following Chronos-expressing ATN or RSC fiber
874 stimuli. RSC input stimulation gives similar variation in latency as ATN inputs. Mann-Whitney
875 U test revealed no significant difference ($p = 0.26$).
876 B, Jitter as a function of latency for ATN and RSC stimuli shows a similar coefficient of
877 variation.
878 C, Decay time constants of EPSCs evoked in layer 3 neurons by stimulating ATN or RSC inputs.
879 Mann-Whitney U test revealed no significant difference ($p = 0.87$).
880 D, E, First oEPSC amplitude as a function of oEPSC half-width (D) and oEPSC rise time (E) for
881 both inputs. We found no clear segregation of oEPSC shapes according to the origin of
882 afferent fibers.
883 F, oEPSPs in a presubicular layer 3 cell, induced by blue or red light stimulation of Chronos-
884 expressing ATN or Chrimson-expressing RSC afferents, respectively.
885 G-J, Comparison of oEPSPs evoked by stimulating ATN or RSC axons, recorded from a same
886 postsynaptic layer 3 presubicular neuron. G, Mean amplitude. H, Maximum rising slope of
887 oEPSPs. I, oEPSPs rise time. $p < 0.05$, Wilcoxon test. J, oEPSPs decay time constants. oEPSPs
888 following ATN and RSC fiber stimulation recorded from the same cell are connected by lines.
889 Dashed lines indicate reversed experimental design (expressing Chronos in RSC and
890 Chrimson in ATN).
891 K, Responses to 10 light stimuli at 20 Hz for ATN and RSC inputs to the same cell.
892 L, Amplitudes of oEPSPs evoked by trains of ATN (left) or RSC (right) fiber stimuli for 11 cells.
893 Dashed lines indicate the reversed experimental design (expressing Chronos in RSC and
894 Chrimson in ATN).
895 M, Summary data from L. On average, the amplitudes of oEPSPs evoked by ATN fiber
896 stimulation were smaller for the fifth than for the first stimulus. oEPSPs evoked by RSC fiber
897 stimulation were similar across five stimuli. Full line, median; Short line, mean; Min to max
898 and quartiles. * $p < 0.05$, Friedman's test and post-hoc Dunn's test comparing each stimulus
899 with the first.
900
901
902 **Figure 3** with 1 supplement.
903 **ATN and RSC axons converge in dorsal presubiculum and contact single layer 3 pyramidal**
904 **neurons.**
905 A, Expression of the blue light sensitive opsin Chronos in ATN and the red light sensitive
906 opsin Chrimson in RSC.
907 B, Axons from ATN (GFP labeled, green) and RSC (tdTomato labeled, red) overlap in layer 1
908 and 3 of dorsal presubiculum. Layer 2 possesses patches of axon-dense and axon-poor
909 zones. RSC fibers avoid axon-dense microstructures formed by ATN fibers in upper layer 3.
910 Scale bar, 200 µm.
911 C, Independent dual wavelength optogenetic stimulation of light sensitive afferent fibers in
912 presubicular slices.
913 D, Two biocytin labeled PrS layer 3 pyramidal cells surrounded by ATN (green) and RSC (red)
914 axons.
915 E, Patch clamp recording from a layer 3 neuron shows optical EPSCs following
916 photostimulation of ATN axons (blue light) and RSC axons (red light).

917 F, 76% of layer 3 pyramidal neurons tested (n = 17 cells/4 mice) received both ATN and RSC
918 input.
919 G, Distributions of putative synaptic contacts from ATN (green) and RSC (red) on the
920 dendrites of three layer 3 neurons. Scale bar 50 µm. The boxed area on Cell 2 is shown in
921 panel I.
922 H, Normalized number of green and red spots for 6 neurons as a function of the distance
923 from soma. Paired values are indicated by dotted lines for the 3 cells in G.
924 I, Examples of ATN-labeled (left), RSC-labeled (middle) and both (right) synapses closely
925 apposed to dendrites of a biocytin-filled layer 3 pyramidal cell. Scale bar 20 µm. Insets show
926 representative high-magnification images. Scale bar 2 µm.
927 See also Figure 3—figure supplement 1.
928
929 **Figure 3—figure supplement 1. Calibration of blue and red light stimulation of Chronos**
930 **and Chrimson.**
931 A, Blue light stimulation of ATN Chronos-expressing fibers evoked oEPSPs in presubicular
932 layer 3 neurons at an intensity of 0.25mW, and 0.5 ms duration of illumination.
933 B, Blue light stimulation at the same intensity and duration did not evoke oEPSPs from RSC
934 Chrimson-expressing fibers.
935 C, D, Response probabilities of presubicular layer 3 cells to stimulation of fibers expressing
936 Chronos or Chrimson with red (C) or blue (D, left) light.
937 E, Experimental design. Injection of AAV5-Chronos-GFP (green) in the ATN, followed by
938 photostimulation combined with patch recording from a presubicular layer 3 cell.
939 F, Amplitudes of oEPSCs evoked in layer 3 cells by blue (0.5 ms, 0.25 mW) or red light (2 ms,
940 0.6 mW) stimuli.
941 G, Representative responses to light stimulation of ATN inputs.
942 H, Injection of AAV5-Chrimson-tdTomato (red) in the RSC, followed by photostimulation
943 combined with patch recording from a presubicular layer 3 cell.
944 I, Amplitudes of oEPSCs evoked in layer 3 cells by blue (0.5 ms, 0.25 mW) or red light (2 ms,
945 0.6 mW) stimuli.
946 J, Representative responses to light stimulation of RSC inputs
947 K, Values and statistical analysis for different stimulation configurations (Panels F and I).
948
949 **Figure 4**.
950 **Supralinear summation of EPSPs and action potential firing following photostimulation of**
951 **ATN and RSC axons.**
952 A, Optical EPSPs in layer 3 neurons in response to blue light activation of ATN axons
953 (cerulean traces), red light activation of RSC axons (purple traces). Supralinear summation of
954 EPSPs following coincident activation of both ATN and RSC axons (black traces). The pink
955 broken line indicates the calculated linear sum of oEPSPs evoked by stimulation of either
956 ATN or RSC axons. Records from cell 1, Fig 3D.
957 B, Amplitudes of dual ATN and RSC oEPSPs plotted as a function of the sum of separate ATN
958 and RSC stimulations (*left*). Each circle is a cell (n = 11 cells/4 mice), Pink line (± 10%)
959 indicates linearity. Pie charts give the number of tested layer 3 neurons with supralinear
960 (grey), linear (pink) or sublinear (white) summation. oEPSPs normalized to linear sum
961 (*bottom right*). Solid circle, Chronos in ATN/Chrimson in RSC, empty circle, Chronos in
962 RSC/Chrimson in ATN. * $p < 0.05$, ** $p < 0.01$, from Wilcoxon test.

963 C, As in B, for dual ATN and RSC oEPSP integrals.
964 D, oEPSPs induced by 20 Hz stimulation of ATN (cerulean), RSC (purple) or both (black). The
965 pink broken line indicates the calculated linear sum of oEPSPs evoked by separate ATN and
966 RSC photostimulation.
967 E, Amplitudes of dual oEPSPs compared to those of the sum of ATN and RSC oEPSPs show
968 that supralinearity increases across 5 stimulations. Two-way ANOVA, $p = 0.0117$. * $p < 0.05$,
969 **** $p < 0.0001$, Šidák's multiple comparison test. # $p < 0.05$, ## $p < 0.01$, Friedman's and
970 *post-hoc* Dunn's test.
971 F, As in E, for dual ATN and RSC oEPSP integrals. Two-way ANOVA, $p = 0.0128$.
972 G, Excitatory postsynaptic responses to photostimulation of ATN (blue light, cerulean traces)
973 or RSC axons (red light, purple traces) or both (blue and red light, black traces) at resting
974 membrane potential (-65 mV) or at a depolarized holding potential (-55 mV). Synaptic
975 excitation led to action potentials when dual ATN and RSC stimuli reached firing threshold.
976 H, Action potential (AP) probability for either or both stimuli at -65 and -55 mV. Data are
977 presented as mean ± SEM.
978 I, Action potentials were induced in presubicular layer 3 neurons by near coincident
979 activation of ATN axons (red light) and RSC axons (blue light). Time delays varied from -50 to
980 +50 ms.
981 J, Firing probability was maximal for short delays between -2 to +5 ms (RSC preceding ATN).
982
983 **Figure 5. EPSP amplifications in layer 3 pyramidal neurons.**
984 A, Optical EPSPs evoked in layer 3 pyramidal neurons following the stimulation of ATN axons
985 (blue light, cerulean traces), RSC axons (red light, purple traces) or both (blue and red light,
986 black traces). Recording pipette contained a cesium gluconate based internal solution and
987 the Na^+ channel blocker QX-314. A large all–or-none EPSP amplification occurred for dual
988 stimuli at 20 Hz, on some trials.
989 B, In the presence of the $GABA_A$ receptor antagonist gabazine (10 µM), dual EPSP
990 amplification occurred earlier in the train.
991 C, The additional presence of the NMDA receptor antagonist APV (100 µM) abolished dual
992 EPSP amplification (black trace). EPSP amplification was partially restored by increasing red
993 light intensity x2 (pale pink traces).
994
995 **Figure 6** with 2 supplements.
996 **Presubicular LMN-projecting layer 4 neurons avoid thalamo-recipient layer 3 and receive**
997 **little direct input from ATN and RSC.**
998 A, Expression of Chronos-GFP in ATN and retrograde labeling of neurons that target LMN.
999 B, Thalamic axons (green) in superficial layers 1 and 3 of presubiculum. Retrobeads label cell
1000 bodies of presubicular layer 4 cells (red).
1001 C, Retrograde rAAV2-tdTomato label cell bodies and dendrites of layer 4 LMN projecting
1002 neurons (red). Apical dendrites of layer 4 pyramidal neurons avoid layer 3 where thalamic
1003 axons ramify.
1004 D, Presubicular slice containing two layer 3 and two layer 4 neurons filled with biocytin
1005 (white) and GFP expressing thalamic axons (green). Scale bar 100 µm. Inset, retrobeads (red)
1006 in the soma of a biocytin filled LMN-projecting layer 4 neuron. Scale bar 10 µm.
1007 E, Layer 3 neurons are regular spiking and layer 4 neurons are burst firing, initially and at
1008 rebound, in reponse to current injection. Black trace, rheobase.
1009 F, T-type Ca^{2+} channel blocker TTA-P2 (1 µM) suppressed burst firing in presubicular layer 4

1010 neurons, while single action potentials were preserved.
1011 G. Representative oEPSCs in layer 3 (left) and layer 4 (right) pyramidal cells, in response to
1012 stimulation of ATN (cerulean) or RSC (purple) inputs.
1013 H, oEPSC latencies in layer 3 and layer 4 cells, for ATN inputs (left, cerulean), or RSC inputs
1014 (right, purple). Each dot is a cell. Same layer 4 cells are indicated by connecting lines, to
1015 show the difference in latency for direct and indirect synaptic responses.
1016 I, oEPSPs in layer 4 neurons in response to stimulation of ATN (cerulean) or RSC (purple)
1017 inputs in control and in the presence of TTX (1 µM) and 4-AP (100 µM). Dashed lines indicate
1018 the timing of the large disynaptic component of the responses (i, indirect), and the small
1019 monosynaptic response (d, direct), isolated in TTX-4AP.
1020 See also Figure 6—figure supplements 1 and 2.
1021
1022
1023 **Figure 6—figure supplement 1. Apical dendrites of presubicular layer 4 neurons avoid the**
1024 **thalamorecipient layer 3.**
1025 A, Retrograde AAV2retro-tdTom was injected in LMN.
1026 B, PrS L4 neuron cell bodies and dendrites were labeled. Scale bar, 50 µm. Full arrowheads,
1027 L4 neurons apical dendrites crossing L3; Empty arrowheads, L4 neurons apical dendrites
1028 skirting L3.
1029 C, Anterograde AAV5-Chronos-GFP was injected in ATN to label thalamic axons, delimiting
1030 PrS layer 3.
1031 D, Examples of biocytin filled layer 4 presubicular neurons. (1) The apical dendrite of this
1032 neuron avoided the densely packed ATN afferents and it didn't show responses to thalamic
1033 stimulations. (2) This neuron's apical dendrite crossed through a short stretch of layer 3
1034 containing ATN afferents, and it responded with low amplitude indirect events. (3) The apical
1035 dendrite of this neuron crossed layer 3 and the zone containing ATN afferents, and was
1036 directly recruited. Scale bar 10µm.
1037 E, AAV-Chronos-GFP injected in ATN, and AAV-Chrimson-tdTom injected in RSC.
1038 F, Image from Figure 7 panel D. Scale bar 100µm.
1039 G, (Left) Enlarged view of dotted area in F, with two labelled L4 neurons. The apical dendrite
1040 of top neuron makes a U-turn to ramify in deep layers and seems to cross path with the axon
1041 of the bottom neuron, potentially forming a synaptic contact. (Right) The dendrite of the top
1042 neuron and axon of bottom neuron are overlayed with pink and green lines respectively.
1043 Scale bar 20µm.
1044
1045 **Figure 6—figure supplement 2. Electrophysiological passive and active intrinsic properties**
1046 **of layer 3 vs. layer 4 neurons.**
1047 Data for layer 3 are summarized in Figure 2—figure supplement 1 and are shown here for
1048 comparison. Statistical differences are indicated as levels of p values (* $p < 0.05$, ** $p < 0.01$,
1049 *** $p < 0.001$, **** $p < 0.0001$) obtained from Mann-Whitney tests between layer 4 ($n = 19$)
1050 and layer 3 ($n = 33$) for each parameter. Box plots indicate maximum and minimum values,
1051 quartiles, full line is the median, short line is the mean.
1052
1053 **Figure 7** with 2 supplements.
1054 **Cross-laminar activation of LMN-projecting layer 4 bursting neurons.**
1055 A, Simultaneous records of a layer 4 and a layer 3 neuron during photostimulation of ATN
1056 afferents. EPSP onset was delayed in the layer 4 neuron. Right panel, expanded view of the

boxed area.
B, Simultaneous records of a layer 4 and a layer 3 neuron during photostimulation of RSC afferents. As in A, layer 4 neurons responded with a delay. Right panel, expanded view of the boxed area.
C, Latencies of synaptic activation indicated by the dotted lines in A, B (ATN stimulation, n = 4 cells; RSC stimulation, n = 1). EPSP onset and AP peak from layer 3 neurons (n = 5). Dotted lines link to the EPSP onset in simultaneously recorded layer 4 neurons (n = 5). $p < 0.05$, Kruskal-Wallis multiple comparison test.
D, Biocytin labeled layer 3 and layer 4 pyramidal neurons, in a presubicular slice containing thalamic (green) and retrosplenial (red) axons. The apical dendrite of one layer 4 neuron makes a U-turn (arrowhead), away from layer 3, where the thalamic axons ramify. The neighboring layer 4 neuron's apical dendrite crosses the thalamo-recipient layer 3 for a short distance before arborizing outside of ATN targeted area, towards the subiculum, on the right. Another biocytin filled layer 4 neuron's dendrites extend toward the deep layers. Scale bar, 100µm.
E, Simultaneous records from a layer 3 and a layer 4 cell to ATN input stimulation (top, 0.25 mW, blue light), ATN and RSC input stimulation (middle, 0.25 mW blue and 0.25 mW red light; light intensities compatible with independent photostimulation) or non-specific ATN and RSC input stimulation (bottom, 3.25 mW blue and 0.25 mW red light). ATN fibers expressed Chronos-GFP (green) and RSC fibers expressed Chrimson-tdTomato (red).
F, Top, oEPSPs and bursts of action potentials in a layer 4 neuron, evoked by dual wavelength stimulation of ATN and RSC afferents at 20 Hz. Amplifications of dual oEPSPs led to firing. Bottom, the NMDA receptor antagonist APV (100 µM) reduced EPSP amplification and prevented action potential firing.
G. Layer 4 bursting neurons are sensitive to the acetylcholine receptor agonist carbachol (10 µM). Action potential firing in response to step current injections in control (black), in the presence of carbachol (grey), and after wash-out (black). Bottom graph, membrane potential depolarization during a 2-minute carbachol application. The number of action potentials increased during the depolarizing steps (i) and on the baseline (ii).
See also Figure 7—figure supplement 1.

Figure 7—figure supplement 1. Regular firing layer 3 vs. intrinsically bursting layer 4 neurons responded to high-intensity light stimulations of ATN or RSC afferents.
Layer 3 neurons respond with single spikes following each light stimulation while layer 4 neurons respond with bursts of action potentials at the beginning of the stimulation train.

Figure 7 – figure supplement 2. Schematic models for landmark anchoring of HD signals.
A, different scenarios with varying degrees of divergence and convergence of the two input sources. We note that matching directional with visual landmark information does not necessarily require synaptic plasticity, and might rely on temporal coincidence.
B, subcellular arrangements of synaptic contacts are important.
C, Inhibitory connectivity is important.

References

1103
1104 Alexander AS, Nitz DA. 2015. Retrosplenial cortex maps the conjunction of internal and
1105 external spaces. Nat Neurosci 18:1143–1151.

1106 Auger SD, Mullally SL, Maguire EA. 2012. Retrosplenial Cortex Codes for Permanent
1107 Landmarks. PLOS ONE 7:e43620.

1108 Balsamo G, Blanco-Hernández E, Liang F, Naumann RK, Coletta S, Burgalossi A, Preston-
1109 Ferrer P. 2022. Modular microcircuit organization of the presubicular head-direction
1110 map. Cell Rep 39, 110684.

1111 Blair HT, Sharp PE. 1995. Anticipatory head direction signals in anterior thalamus: evidence
1112 for a thalamocortical circuit that integrates angular head motion to compute head
1113 direction. J Neurosci 15:6260–6270.

1114 Boccara CN, Sargolini F, Thoresen VH, Solstad T, Witter MP, Moser EI, Moser M-B. 2010. Grid
1115 cells in pre- and parasubiculum. Nat Neurosci 13:987–994.

1116 Boehm J, Kang M-G, Johnson RC, Esteban J, Huganir RL, Malinow R. 2006. Synaptic
1117 incorporation of AMPA receptors during LTP is controlled by a PKC phosphorylation
1118 site on GluR1. Neuron. 51:213–225.

1119 Calton JL, Stackman RW, Goodridge JP, Archey WB, Dudchenko PA, Taube JS. 2003.
1120 Hippocampal place cell instability after lesions of the head direction cell network. J
1121 Neurosci 23:9719–9731.

1122 Clark BJ, Bassett JP, Wang SS, Taube JS. 2010. Impaired Head Direction Cell Representation in
1123 the Anterodorsal Thalamus after Lesions of the Retrosplenial Cortex. J Neurosci
1124 30:5289–5302.

1125 Fallahnezhad M, Le Mero J, Zenelaj X, Vincent J, Rochefort C, Rondi-Reig L. 2023. Cerebellar
1126 control of a unitary head direction sense. Proc Natl Acad Sci U S A 120:e2214539120.

1127 Fisher YE, Marquis M, D'Alessandro I, Wilson RI. 2022. Dopamine promotes head direction
1128 plasticity during orienting movements. Nature 612:316–322.

1129 Fricker D, Miles R. 2000. EPSP amplification and the precision of spike timing in hippocampal
1130 neurons. Neuron. 28:559–569.

1131 Fricker D, Dinocourt C, Eugène E, Wood JN, Wood J, Miles R. 2009. Pyramidal cells of rodent
1132 presubiculum express a tetrodotoxin-insensitive Na+ current. J Physiol 587:4249–
1133 4264.

1134 Gil Z, Connors BW, Amitai Y. 1999. Efficacy of thalamocortical and intracortical synaptic
1135 connections: quanta, innervation, and reliability. Neuron 23:385–397.

1136 Goodridge JP, Taube JS. 1997. Interaction between the postsubiculum and anterior thalamus
1137 in the generation of head direction cell activity. J Neurosci 17:9315–9330.

1138 Häusser M, Mel B. 2003. Dendrites: bug or feature? Current Opinion in Neurobiology.
1139 13:372–383.

1140 Hedrick NG, Lu Z, Bushong E, Singhi S, Nguyen P, Magaña Y, Jilani S, Lim BK, Ellisman M,
1141 Komiyama T. 2022. Learning binds new inputs into functional synaptic clusters via
1142 spinogenesis. Nat Neurosci 25:726–737.

1143 Hooks BM, Lin JY, Guo C, Svoboda K. 2015. Dual-channel circuit mapping reveals
1144 sensorimotor convergence in the primary motor cortex. Journal of Neuroscience.
1145 35:4418–4426.

Huang L-W, Simonnet J, Nassar M, Richevaux L, Lofredi R, Fricker D. 2017. Laminar Localization and Projection-Specific Properties of Presubicular Neurons Targeting the Lateral Mammillary Nucleus, Thalamus, or Medial Entorhinal Cortex. eneuro 4:ENEURO.0370-16.2017.

Ishihara Y, Fukuda T. 2016. Immunohistochemical investigation of the internal structure of the mouse subiculum. NSC. 337:1–25.

Jacob P-Y, Casali G, Spieser L, Page H, Overington D, Jeffery K. 2017. An independent, landmark-dominated head-direction signal in dysgranular retrosplenial cortex. Nat Neurosci 20:173–175.

Jeffery KJ, Page HJI, Stringer SM. 2016. Optimal cue combination and landmark-stability learning in the head direction system. J Physiol. Lond). 594:6527–6534.

Jones BF, Witter MP. 2007. Cingulate cortex projections to the parahippocampal region and hippocampal formation in the rat. Hippocampus 17:957–976.

Keshavarzi S, Bracey EF, Faville RA, Campagner D, Tyson AL, Lenzi SC, Branco T, Margrie TW. 2022. Multisensory coding of angular head velocity in the retrosplenial cortex. Neuron 110:532-543.e9.

Klapoetke NC et al. 2014. Independent optical excitation of distinct neural populations. Nat Methods 11:338–346.

Knierim JJ, Zhang K. 2012. Attractor dynamics of spatially correlated neural activity in the limbic system. Annu Rev Neurosci 35:267–285.

Kononenko NL, Witter MP. 2012. Presubiculum layer III conveys retrosplenial input to the medial entorhinal cortex. Hippocampus 22:881–895.

Larkum ME, Zhu JJ, Sakmann B. 1999. A new cellular mechanism for coupling inputs arriving at different cortical layers. Nature 398, 338–341.

Larkum ME, Waters J, Sakmann B, Helmchen F. 2007. Dendritic spikes in apical dendrites of neocortical layer 2/3 pyramidal neurons. J. Neurosci. 27, 8999–9008.

Larkum ME, Nevian T, Sandler M, Polsky A, Schiller J. 2009. Synaptic Integration in Tuft Dendrites of Layer 5 Pyramidal Neurons: A New Unifying Principle. Science 325, 756–760.

Lavzin M, Rapoport S, Polsky A, Garion L, Schiller J. 2012. Nonlinear dendritic processing determines angular tuning of barrel cortex neurons in vivo. Nature. 490:397–401.

Liu J, Kashima T, Morikawa S, Noguchi A, Ikegaya Y, Matsumoto N. 2021. Molecular characterization of superficial layers of the presubiculum during development. Front Neuroanat 15.

Makarov R, Pagkalos M, Poirazi P. 2023. Dendrites and Efficiency: Optimizing Performance and Resource Utilization. https://arxiv.org/abs/2306.07101.

Martin LJ, Blackstone CD, Levey AI, Huganir RL, Price DL. 1993. AMPA glutamate receptor subunits are differentially distributed in rat brain. NSC. 53:327–358.

Mathon B, Nassar M, Simonnet J, Le Duigou C, Clemenceau S, Miles R, Fricker D. 2015. Increasing the effectiveness of intracerebral injections in adult and neonatal mice: a neurosurgical point of view. Neurosci Bull 31:685–696.

McNaughton BL, Battaglia FP, Jensen O, Moser EI, Moser M-B. 2006. Path integration and the neural basis of the “cognitive map.” Nat Rev Neurosci 7:663–678.

Mel BW. Synaptic integration in an excitable dendritic tree. 1993. J Neurophysiol. 70(3):1086-101.

Milstein AD, Bloss EB, Apostolides PF, Vaidya SP, Dilly GA, Zemelman BV, Magee JC. 2015. Inhibitory Gating of Input Comparison in the CA1 Microcircuit. Neuron 87:1274–1289.

Mitchell AS, Czajkowski R, Zhang N, Jeffery KJ, Nelson AJD. 2018. Retrosplenial cortex and its role in spatial cognition. Brain and Neuroscience Advances. 8:586.

Nassar M, Simonnet J, Huang L-W, Mathon B, Cohen I, Bendels MHK, Beraneck M, Miles R, Fricker D. 2018. Anterior Thalamic Excitation and Feedforward Inhibition of Presubicular Neurons Projecting to Medial Entorhinal Cortex. J Neurosci 38:6411–6425.

Naud R, Friedenberger Z, Toth K. 2023. Silences, Spikes and Bursts: Three-Part Knot of the Neural Code. arXiv:2302.07206v1. 1–15.

Page HJI, Jeffery KJ. Landmark-Based Updating of the Head Direction System by Retrosplenial Cortex: A Computational Model. Front Cell Neurosci. 2018 Jul 13;12:191. doi: 10.3389/fncel.2018.00191.

Payeur A, Guerguiev J, Zenke F, Richards BA, Naud R. 2021. Burst-dependent synaptic plasticity can coordinate learning in hierarchical circuits. Nat Neurosci 24:1010–1019.

Peng Y, Barreda Tomás FJ, Klisch C, Vida I, Geiger JRP. 2017. Layer-Specific Organization of Local Excitatory and Inhibitory Synaptic Connectivity in the Rat Presubiculum. Cereb Cortex. 27:2435-2452.

Peyrache A, Lacroix MM, Petersen PC, Buzsáki G. 2015. Internally organized mechanisms of the head direction sense. Nat Neurosci 18:569–575.

Poirazi P, Brannon T, Mel BW. 2003. Arithmetic of subthreshold synaptic summation in a model CA1 pyramidal cell. Neuron. 37(6):977-87.

Poirazi P, Papoutsi A. 2020. Illuminating dendritic function with computational models. Nat Rev Neurosci 1–19.

Polsky A, Mel BW, Schiller J. 2004. Computational subunits in thin dendrites of pyramidal cells. Nat Neurosci 7:621–627.

Porter JT, Cauli B, Tsuzuki K, Lambolez B, Rossier J, Audinat E. 1999. Selective excitation of subtypes of neocortical interneurons by nicotinic receptors. J Neurosci 19:5228–5235.

Preston-Ferrer P, Coletta S, Frey M, Burgalossi A. 2016. Anatomical organization of presubicular head-direction circuits. eLife 5.

Ranck JB. 1984. Head direction cells in the deep layer of dorsal presubiculum in freely moving rats. Soc Neurosci Abstr.

Rees CL, Moradi K, Ascoli GA. 2017. Weighing the Evidence in Peters' Rule: Does Neuronal Morphology Predict Connectivity? Trends Neurosci 40:63–71.

Richevaux L, Schenberg L, Beraneck M, Fricker D. 2019. In Vivo Intracerebral Stereotaxic Injections for Optogenetic Stimulation of Long-Range Inputs in Mouse Brain Slices. JoVE J Vis Exp e59534.

Shibata H, Honda Y. 2012. Thalamocortical projections of the anterodorsal thalamic nucleus in the rabbit. J Comp Neurol 520:2647–2656.

1232 Siegenthaler D, Denny H, Skromne Carrasco S, Mayer JL, Levenstein D, Peyrache A, Trenholm
1233 S, Macé E. 2024. Visual objects refine head direction coding. bioRxiv
1234 2024.10.21.619417; doi: https://doi.org/10.1101/2024.10.21.619417

1235 Simonnet J, Eugène E, Cohen I, Miles R, Fricker D. 2013. Cellular neuroanatomy of rat
1236 presubiculum. Eur J Neurosci 37:583–597.

1237 Simonnet J, Nassar M, Stella F, Cohen I, Mathon B, Boccara CN, Miles R, Fricker D. 2017.
1238 Activity dependent feedback inhibition may maintain head direction signals in mouse
1239 presubiculum. Nat Commun 8:16032.

1240 Simonnet J, Richevaux L, Fricker D. 2021. Single or Double Patch-Clamp Recordings In Ex Vivo
1241 Slice Preparation: Functional Connectivity, Synapse Dynamics, and Optogenetics.
1242 Methods Mol Biol Clifton NJ 2188:285–309.

1243 Sit KK, Goard MJ. 2023. Coregistration of heading to visual cues in retrosplenial cortex. Nat
1244 Commun 14:1992.

1245 Skaggs WE, Knierim JJ, Kudrimoti HS, McNaughton BL. 1995. A model of the neural basis of
1246 the rat's sense of direction. Adv Neural Inf Process Syst 7:173–180.

1247 Slomianka L, Geneser FA. 1991. Distribution of acetylcholinesterase in the hippocampal
1248 region of the mouse: I. Entorhinal area, parasubiculum, retrosplenial area, and
1249 presubiculum. J Comp Neurol 303:339–354.

1250 Smith SL, Smith IT, Branco T, Häusser M. 2013. Dendritic spikes enhance stimulus selectivity
1251 in cortical neurons in vivo. Nature. 503:115–120.

1252 Spruston N. Pyramidal neurons: dendritic structure and synaptic integration. 2008. Nat Rev
1253 Neurosci. 9(3):206-21.

1254 Stackman RW, Taube JS. 1998. Firing properties of rat lateral mammillary single units: head
1255 direction, head pitch, and angular head velocity. J Neurosci 18:9020–9037.

1256 Sugar J, Witter MP. 2016. Postnatal development of retrosplenial projections to the
1257 parahippocampal region of the rat. eLife 5.

1258 Takahashi N, Oertner TG, Hegemann P, Larkum ME. 2016. Active cortical dendrites modulate
1259 perception. Science 354:1587–1590.

1260 Takahashi N, Ebner C, Sigl-Glöckner J, Moberg S, Nierwetberg S, Larkum ME. 2020. Active
1261 dendritic currents gate descending cortical outputs in perception. Nat Neurosci.
1262 54:677–679.

1263 Taube JS. 1995. Head direction cells recorded in the anterior thalamic nuclei of freely moving
1264 rats. J Neurosci 15:70–86.

1265 Taube JS, Muller RU, Ranck JB. 1990a. Head-direction cells recorded from the postsubiculum
1266 in freely moving rats. I. Description and quantitative analysis. J Neurosci 10:420–435.

1267 Taube JS, Muller RU, Ranck JB. 1990b. Head-direction cells recorded from the postsubiculum
1268 in freely moving rats. II. Effects of environmental manipulations. J Neurosci 10:436–
1269 447.

1270 Tukker JJ, Tang Q, Burgalossi A, Brecht M. 2015. Head-Directional Tuning and Theta
1271 Modulation of Anatomically Identified Neurons in the Presubiculum. Journal of
1272 Neuroscience. 35:15391–15395.

1273 Van der Goes M-SH, Voigts J, Newman JP, Toloza EHS, Brown NJ, Murugan P, Harnett MT.
1274 2022. Coordinated Head Direction Representations in Mouse Anterodorsal Thalamic

Nucleus and Retrosplenial Cortex. bioRxiv doi.org/10.1101/2022.08.20.504604.

Van Groen T, Wyss JM. 2003. Connections of the retrosplenial granular b cortex in the rat. J Comp Neurol 463:249–263.

Van Groen T, Wyss JM. 1992. Connections of the retrosplenial dysgranular cortex in the rat. J Comp Neurol 315:200–216.

Van Groen T, Wyss JM. 1990a. The connections of presubiculum and parasubiculum in the rat. Brain Res 518:227–243.

Van Groen T, Wyss JM. 1990b. Connections of the retrosplenial granular a cortex in the rat. J Comp Neurol 300:593–606.

Van Groen T, Wyss JM. 1990c. The postsubicular cortex in the rat: characterization of the fourth region of the subicular cortex and its connections. Brain Res 529:165–177.

Vann SD, Aggleton JP, Maguire EA. 2009. What does the retrosplenial cortex do? Nat Rev Neurosci. 10:792–802.

Vedder LC, Miller AMP, Harrison MB, Smith DM. 2017. Retrosplenial Cortical Neurons Encode Navigational Cues, Trajectories and Reward Locations During Goal Directed Navigation. Cereb Cortex. 2017; 27(7):3713-3723.

Vogt BA, Miller MW. 1983. Cortical connections between rat cingulate cortex and visual, motor, and postsubicular cortices. J Comp Neurol 216:192–210.

Whittington JCR, Dorrell W, Behrens TEJ, Ganguli S, El-Gaby M. 2025. A tale of two algorithms: Structured slots explain prefrontal sequence memory and are unified with hippocampal cognitive maps. Neuron, Volume 113, Issue 2, 321 - 333.e6.

Wilson DE, Whitney DE, Scholl B, Fitzpatrick D. 2016. Orientation selectivity and the functional clustering of synaptic inputs in primary visual cortex. Nat Neurosci. 19:1003–1009.

Yan Y, Burgess N, Bicanski A. A model of head direction and landmark coding in complex environments. PLoS Comput Biol. 2021 Sep 27;17(9):e1009434. doi: 10.1371/journal.pcbi.1009434.

Yoder RM, Peck JR, Taube JS. 2015. Visual landmark information gains control of the head direction signal at the lateral mammillary nuclei. J Neurosci 35:1354–1367.

Yoder RM, Taube JS. 2011. Projections to the anterodorsal thalamus and lateral mammillary nuclei arise from different cell populations within the postsubiculum: implications for the control of head direction cells. Hippocampus 21:1062–1073.

Yoder RM, Chan JHM, Taube JS. 2017. Acetylcholine Contributes to the Integration of Self-Movement Cues in Head Direction Cells. Behav Neurosci 131:312-324.

Yoder RM, Valerio S, Crego ACG, Clark BJ, Taube JS. 2019. Bilateral postsubiculum lesions impair visual and nonvisual homing performance in rats. Behav Neurosci 133:496–507.

Zugaro MB, Arleo A, Berthoz A, Wiener SI. 2003. Rapid spatial reorientation and head direction cells. J Neurosci 23:3478–3482.

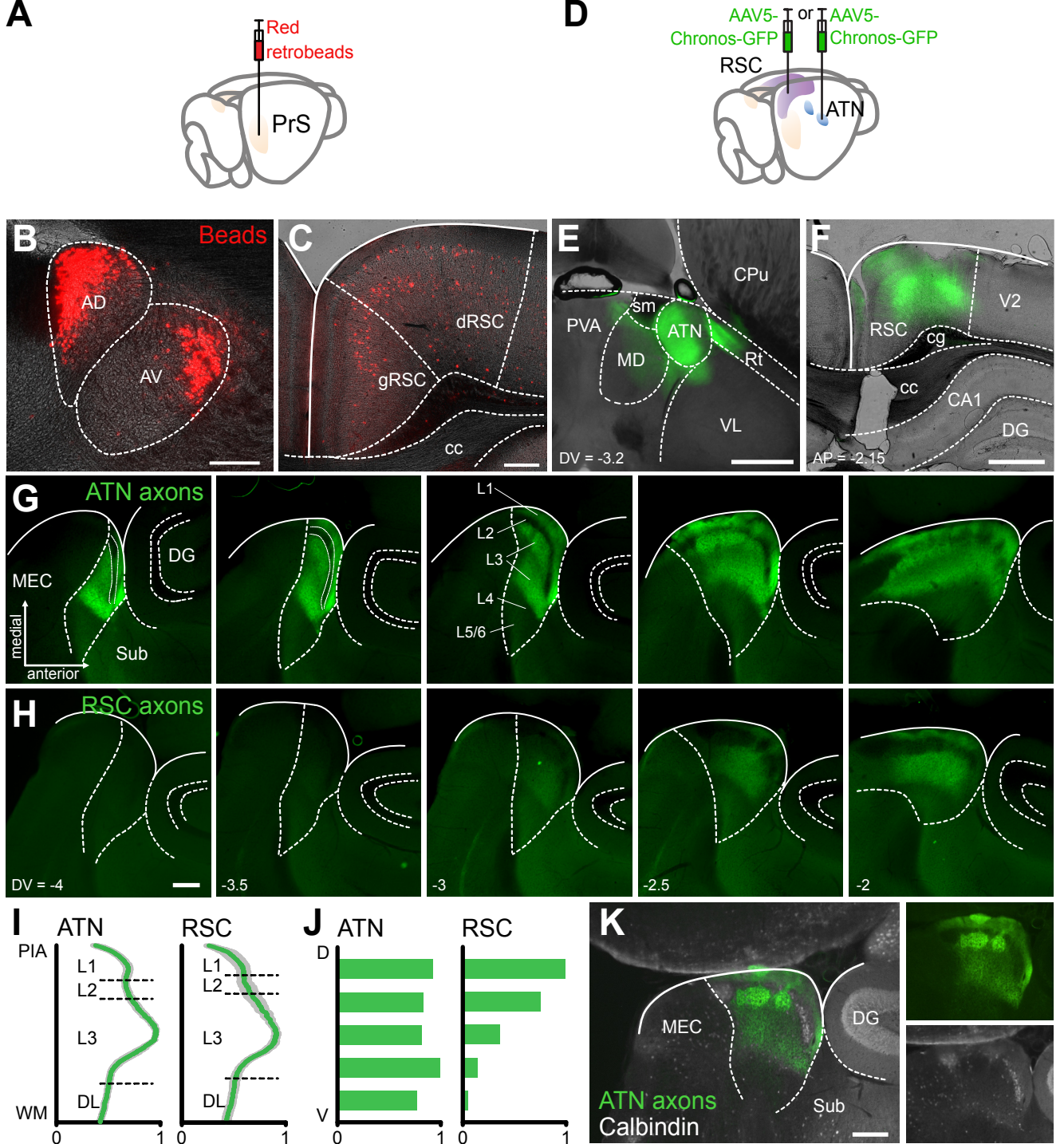
A
Red
retrobeads
PrS
D
AAV5-
Chronos-GFP
or
AAV5-
Chronos-GFP
RSC
ATN
B
Beads
AD
AV
C
dRSC
gRSC
cc
E
CPu
sm
PVA
ATN
MD
Rt
VL
DV = -3.2
F
V2
RSC
cg
cc
CA1
DG
AP = -2.15
G
ATN axons
DG
MEC
medial
anterior
Sub
L1
L2
L3
L4
L5/6
H
RSC axons
DV = -4
-3.5
-3
-2.5
-2
I
ATN
RSC
PIA
L1
L2
L3
DL
WM
0
1
J
ATN
RSC
D
V
0
1
K
MEC
DG
ATN axons
Calbindin
Sub

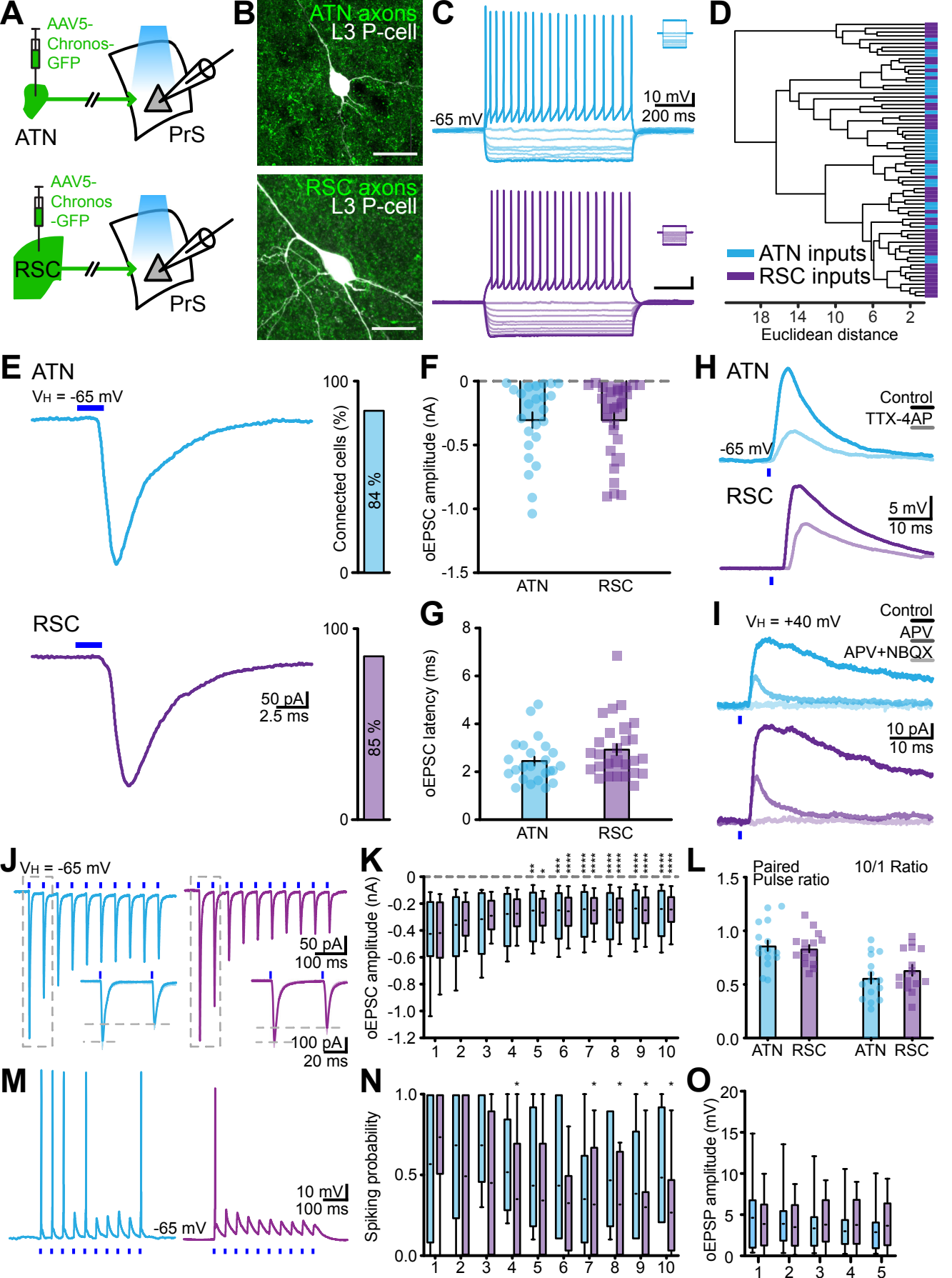
A
AAV5-
Chronos-
GFP
ATN
PrS
AAV5-
Chronos
-GFP
RSC
PrS
B
ATN axons
L3 P-cell
RSC axons
L3 P-cell
C
-65 mV
10 mV
200 ms
D
ATN inputs
RSC inputs
18
14
10
6
2
Euclidean distance
E
ATN
VH = -65 mV
Connected cells (%)
100
0
84 %
RSC
50 pA
2.5 ms
85 %
F
oEPSC amplitude (nA)
0
-0.5
-1.0
-1.5
ATN
RSC
G
oEPSC latency (ms)
8
6
4
2
0
ATN
RSC
H
ATN
Control
TTX-4AP
-65 mV
RSC
5 mV
10 ms
I
VH = +40 mV
Control
APV
APV+NBQX
10 pA
10 ms
J
VH = -65 mV
50 pA
100 ms
100 pA
20 ms
K
oEPSC amplitude (nA)
0
-0.2
-0.4
-0.6
-0.8
-1.0
-1.2
1
2
3
4
5
6
7
8
9
10
L
Paired
Pulse ratio
10/1 Ratio
1.5
1.0
0.5
0.0
ATN
RSC
ATN
RSC
M
10 mV
100 ms
-65 mV
N
Spiking probability
1.0
0.5
0.0
1
2
3
4
5
6
7
8
9
10
O
oEPSP amplitude (mV)
20
15
10
5
0
1
2
3
4
5

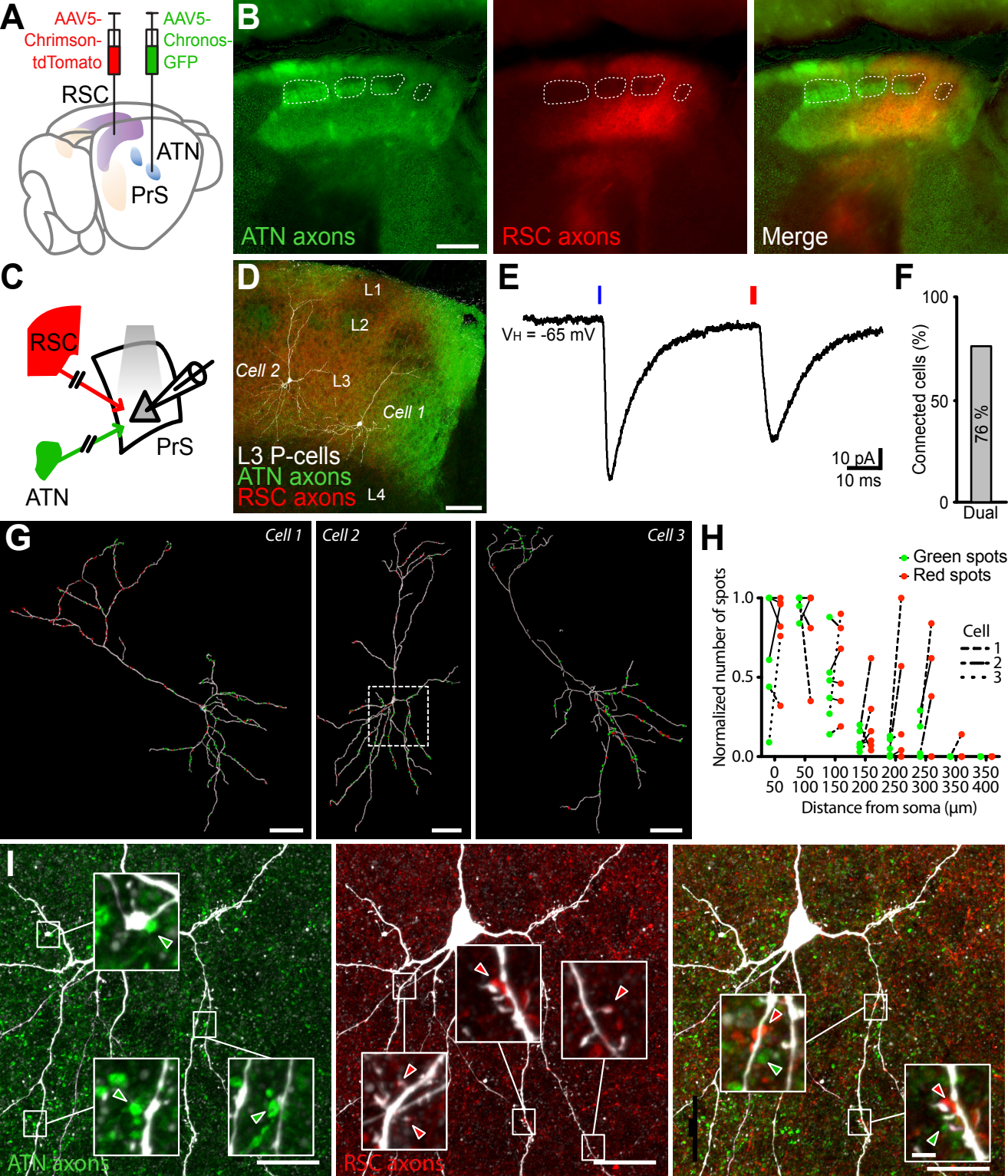
A
AAV5-
Chrimson-
tdTomato
AAV5-
Chronos-
GFP
RSC
ATN
PrS
B
ATN axons
RSC axons
Merge
C
RSC
PrS
ATN
D
L1
L2
L3
L4
Cell 2
Cell 1
L3 P-cells
ATN axons
RSC axons
E
VH = -65 mV
10 pA
10 ms
F
Connected cells (%)
100
50
0
76 %
Dual
G
Cell 1
Cell 2
Cell 3
H
Green spots
Red spots
Normalized number of spots
1.0
0.5
0.0
Cell
1
2
3
0 50 100 150 200 250 300 350
50 100 150 200 250 300 350 400
Distance from soma (µm)
I
ATN axons
RSC axons

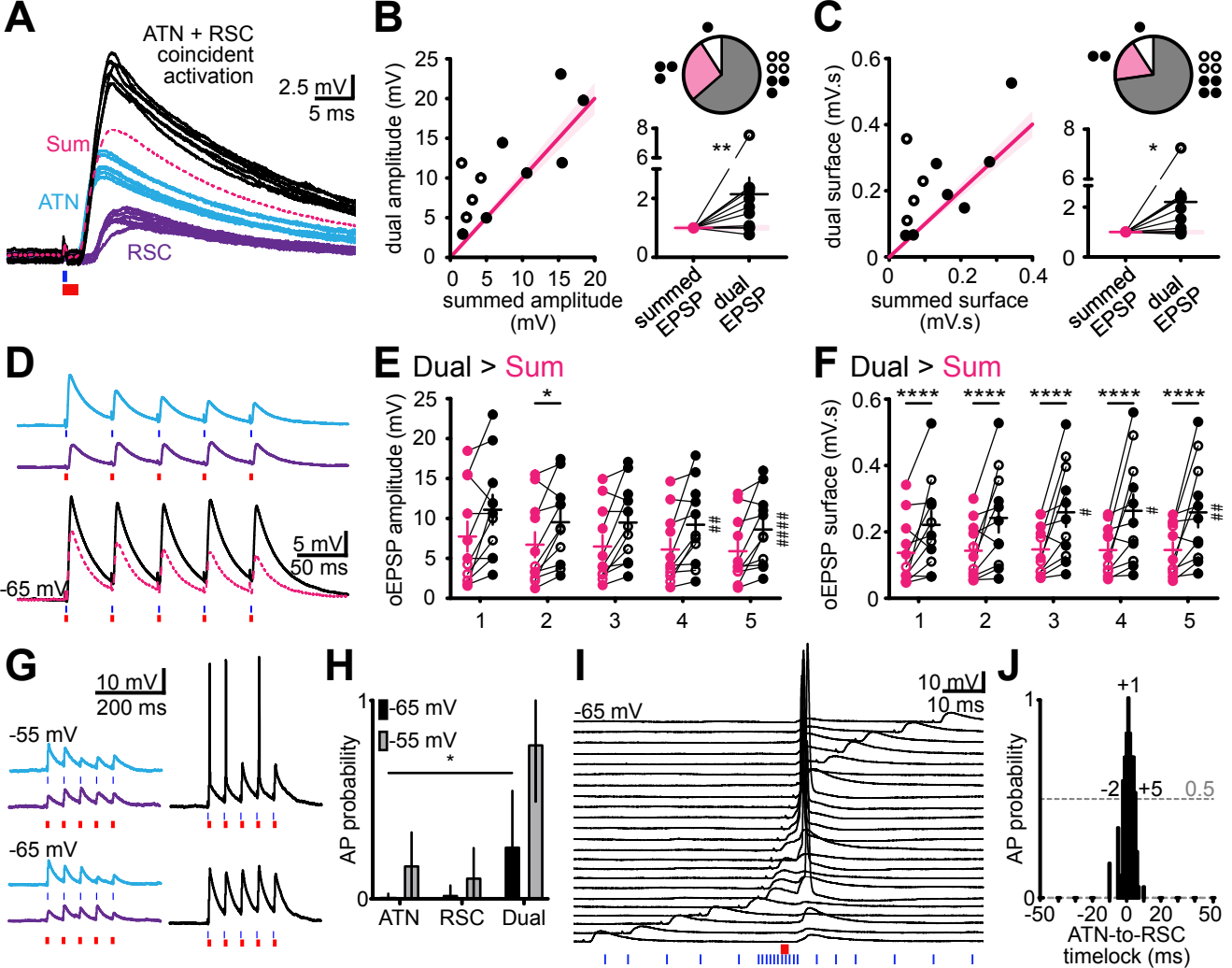
A
ATN + RSC
coincident
activation
2.5 mV
5 ms
Sum
ATN
RSC
B
dual amplitude (mV)
summed amplitude
(mV)
summed
EPSP
dual
EPSP
C
dual surface (mV.s)
summed surface
(mV.s)
summed
EPSP
dual
EPSP
D
5 mV
50 ms
-65 mV
E Dual > Sum
oEPSP amplitude (mV)
F Dual > Sum
oEPSP surface (mV.s)
G
10 mV
200 ms
-55 mV
-65 mV
H
-65 mV
-55 mV
AP probability
ATN
RSC
Dual
I
-65 mV
10 mV
10 ms
J
+1
-2
+5
0.5
AP probability
ATN-to-RSC
timelock (ms)

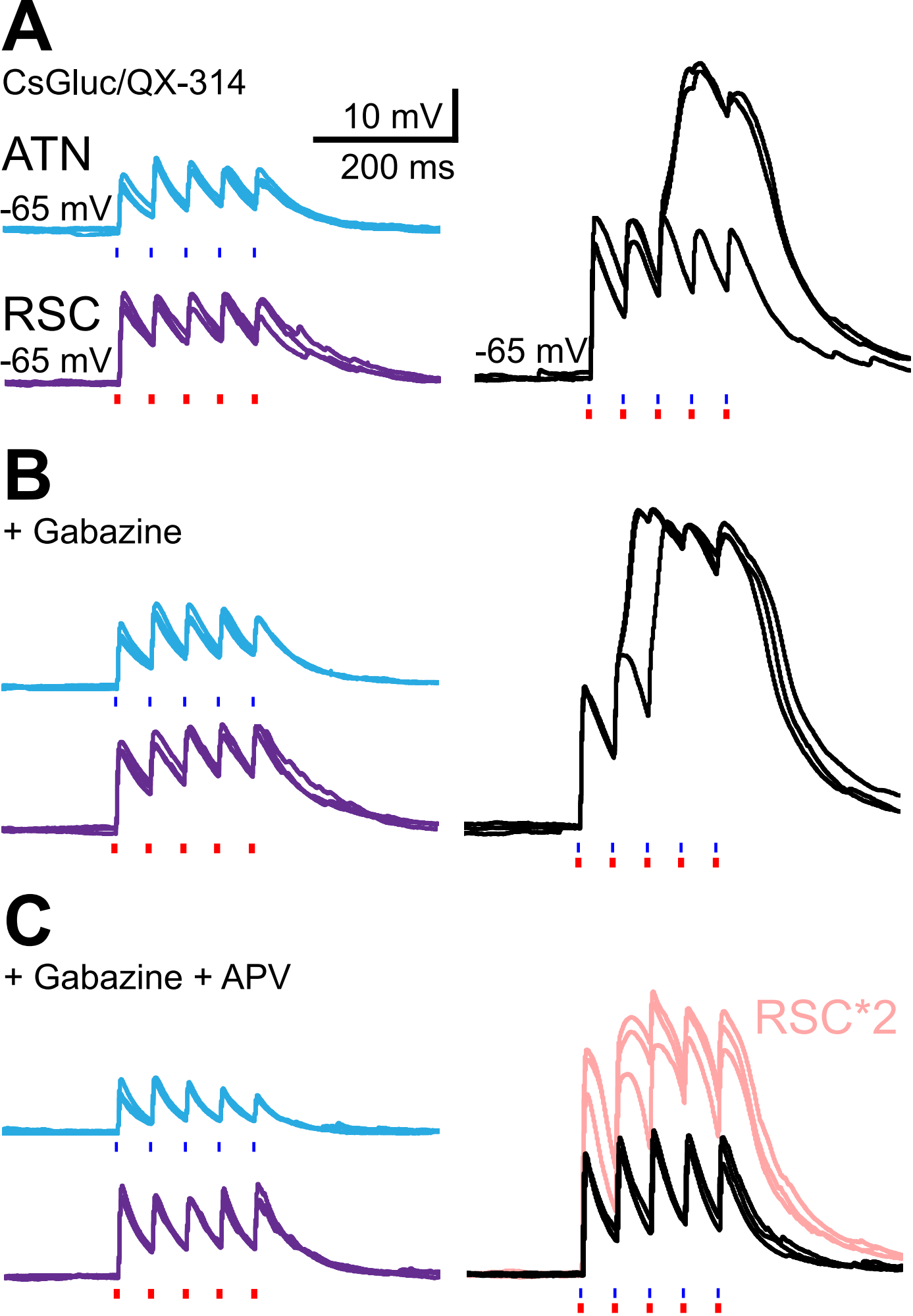
A
CsGluc/QX-314
10 mV
200 ms
ATN
-65 mV
RSC
-65 mV
-65 mV
B
+ Gabazine
C
+ Gabazine + APV
RSC*2

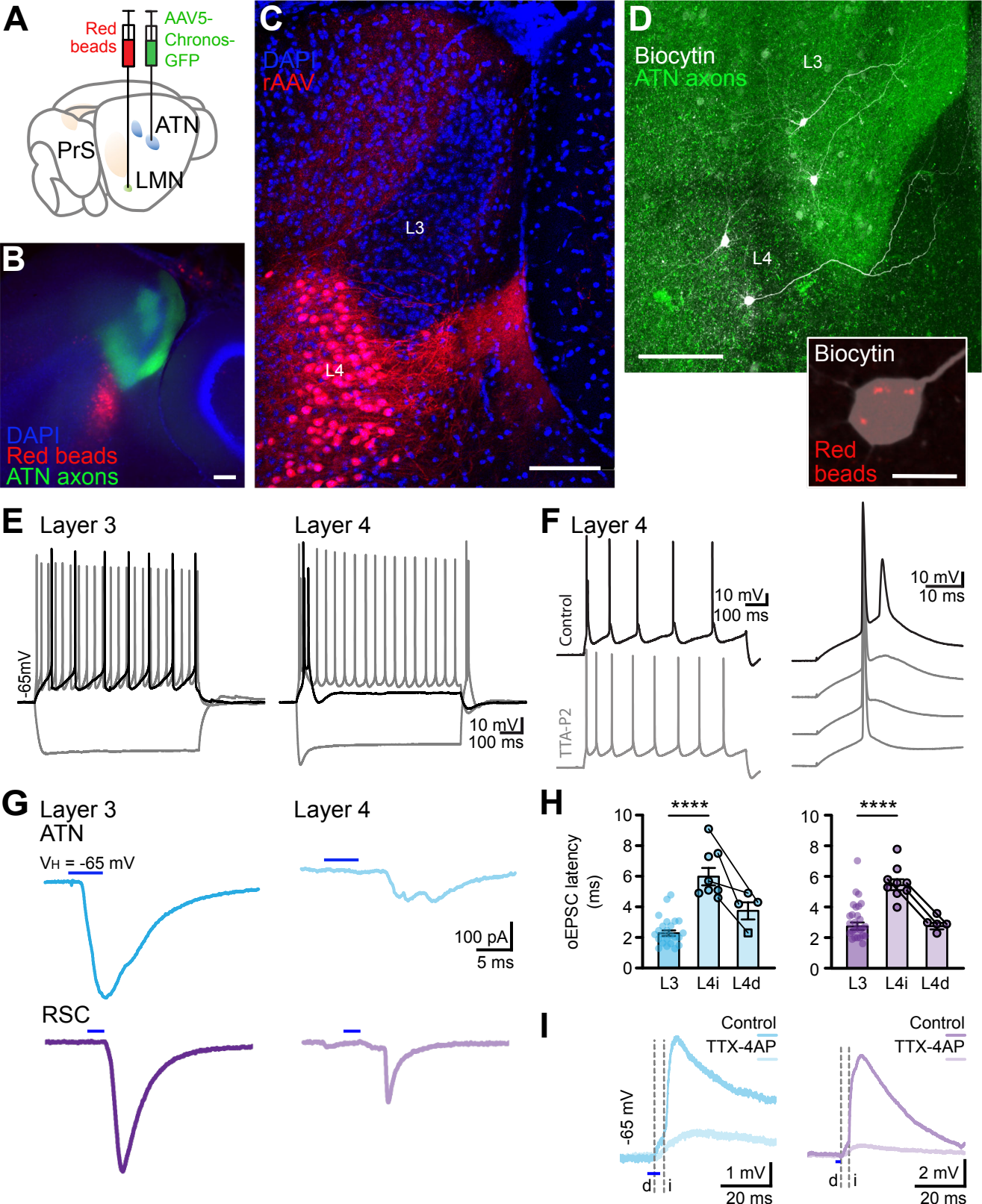
A
Red beads
AAV5-Chronos-GFP
ATN
PrS
LMN
B
DAPI
Red beads
ATN axons
C
DAPI
rAAV
L3
L4
D
Biocytin
ATN axons
L3
L4
Biocytin
Red beads
E
Layer 3
Layer 4
-65mV
10 mV
100 ms
F
Layer 4
Control
TTA-P2
10 mV
100 ms
10 mV
10 ms
G
Layer 3
ATN
VH = -65 mV
Layer 4
100 pA
5 ms
RSC
H
oEPSC latency (ms)
****
****
L3
L4i
L4d
I
Control
TTX-4AP
-65 mV
d
i
1 mV
20 ms
2 mV
20 ms

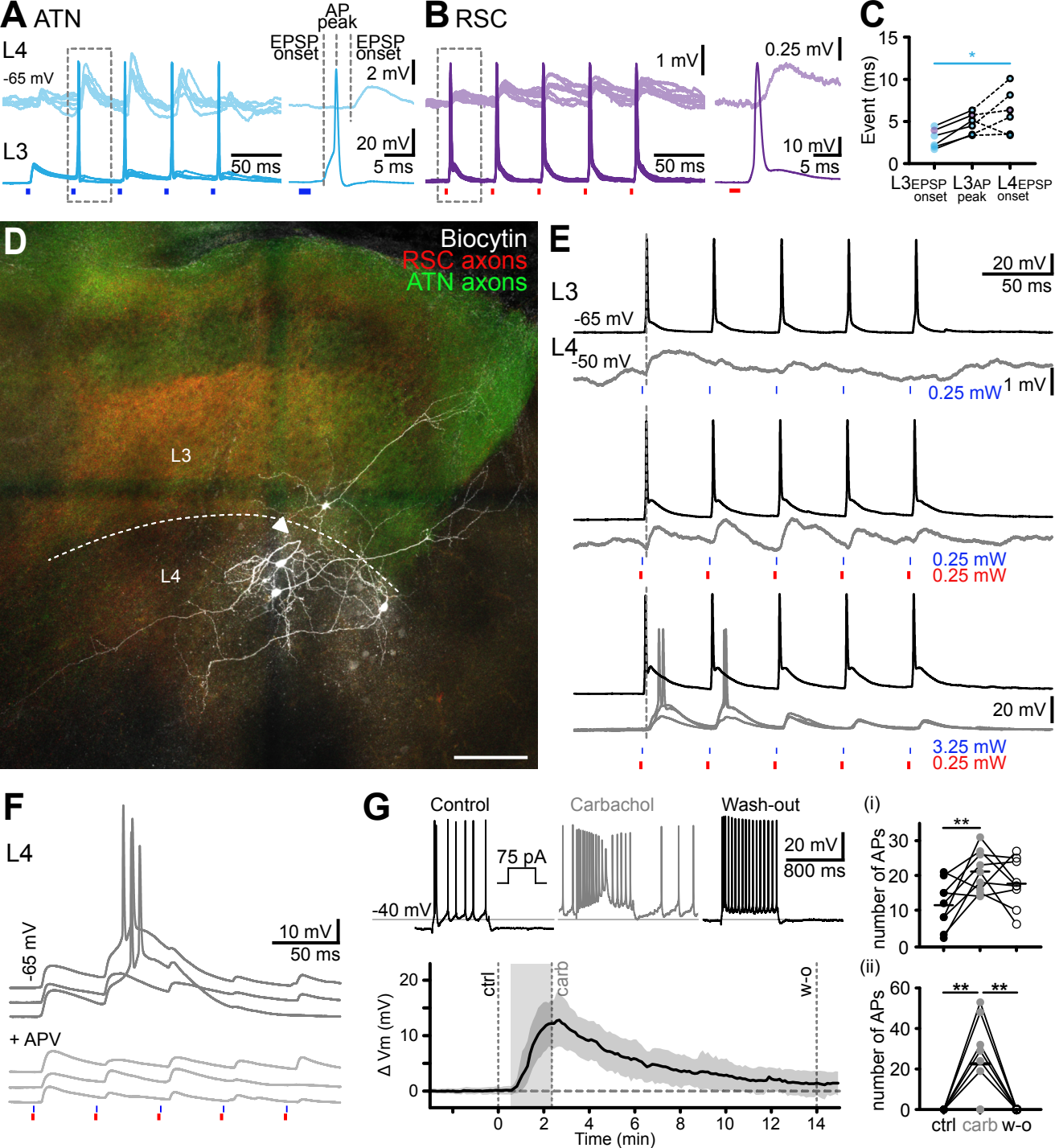
A ATN
L4
-65 mV
L3
EPSP onset
AP peak
EPSP onset
2 mV
20 mV
5 ms
50 ms
B RSC
1 mV
0.25 mV
10 mV
5 ms
50 ms
C
Event (ms)
L3EPSP onset
L3AP peak
L4EPSP onset
D
Biocytin
RSC axons
ATN axons
L3
L4
E
L3
-65 mV
L4
-50 mV
20 mV
50 ms
0.25 mW
1 mV
0.25 mW
0.25 mW
20 mV
3.25 mW
0.25 mW
F
L4
-65 mV
10 mV
50 ms
+ APV
G
Control
Carbachol
Wash-out
75 pA
-40 mV
20 mV
800 ms
(i)
number of APs
(ii)
number of APs
ctrl
carb
w-o
Δ Vm (mV)
Time (min)